Research

Check for updates

Author for correspondence:
Mike Lockwood
e-mail: m.lockwood@reading.ac.uk

Placing limits on long-term variations in quiet-Sun irradiance and their contribution to total solar irradiance and solar radiative forcing of climate

Mike Lockwood[1] and William T. Ball[2]

[1]Department of Meteorology, University of Reading, Reading, UK
[2]Department of Geoscience and Remote Sensing, T.U. Delft, Delft, The Netherlands

ML, 0000-0002-7397-2172

Recent reconstructions of total solar irradiance (TSI) postulate that quiet-Sun variations could give significant changes to the solar power input to Earth's climate (radiative climate forcings of 0.7–$1.1\,\mathrm{W\,m^{-2}}$ over 1700–2019) arising from changes in quiet-Sun magnetic fields that have not, as yet, been observed. Reconstructions without such changes yield solar forcings that are smaller by a factor of more than 10. We study the quiet-Sun TSI since 1995 for three reasons: (i) this interval shows rapid decay in average solar activity following the grand solar maximum in 1985 (such that activity in 2019 was broadly equivalent to that in 1900); (ii) there is improved consensus between TSI observations; and (iii) it contains the first modelling of TSI that is independent of the observations. Our analysis shows that the most likely upward drift in quiet-Sun radiative forcing since 1700 is between $+0.07$ and $-0.13\,\mathrm{W\,m^{-2}}$. Hence, we cannot yet discriminate between the quiet-Sun TSI being enhanced or reduced during the Maunder and Dalton sunspot minima, although there is a growing consensus from the combinations of models and observations that it was slightly enhanced. We present reconstructions that add quiet-Sun TSI and its uncertainty to models that reconstruct the effects of sunspots and faculae.

THE ROYAL SOCIETY
PUBLISHING

1. Introduction

Comprehensive reviews of the potential influences of solar variability of climate have been presented in recent years by Gray *et al.* [1], Solanki *et al.* [2] and Owens *et al.* [3]. The present paper addresses one factor not discussed much in those reviews, namely potential variations in the quiet-Sun contribution to total solar irradiance (TSI). The term 'quiet Sun' refers to the relatively featureless areas of the visible solar surface (the photosphere) where there is no detected magnetic field threading the surface that can alter the emission of the surface; hence, it is the part of the solar surface that is separate and distinct from any magnetic features such as sunspots, active region faculae, network faculae and ephemeral flux. We have very little reliable information on variations of the quiet Sun, but recent papers postulating their existence have derived significant solar radiative climate forcings (e.g. [4,5]). It should be stressed that neither the postulated quiet-Sun irradiance variations nor the causal magnetic fields have, as yet, been detected. In this paper, we use recent data to place limits on the effect of the quiet Sun and show that it is below the measurement uncertainties.

(a) Total solar irradiance observations

The TSI is the solar electromagnetic power, integrated over all wavelengths and per unit cross-sectional area, reaching Earth. The absolute radiometry needed to measure TSI is exceptionally challenging. To avoid atmospheric effects, such measurements are made by instruments on board spacecraft, which adds considerably to the difficulties of calibrating the instruments to the precise accuracies required and of maintaining the required long-term stability of those calibrations. An early example was the Hickey–Frieden (H–F) Cavity Radiometer on board the Nimbus-7/Earth Radiation Budget (ERB) spacecraft [6,7]. Corrections for sensitivity drifts are needed because exposure to high-energy solar radiation, temperature fluctuations and high-energy particles modify the interior surfaces of the radiometer cavity. There are other effects, for example of large thermal fluctuations on the instrument electronics, that need to be accounted for and Nimbus-7 was prone to pointing direction glitches. As a single instrument on ERB, calibration of the data was only possible using data from instruments on other craft operating at the same time, which were not always available and that have their own calibration uncertainties [8]. The subsequent generation of radiometer instrumentation, such as the Active Cavity Radiometer Irradiance Monitor (ACRIM) detectors, radically reduced the degradation problem by having two radiometers: one used routinely and the other used sparingly and therefore degrading to a much smaller degree. From the comparison of the two, the degradation of both can be computed with the assumption that the degradation, as a function of the amount of use, is the same in both radiometers (see [9]).

Because TSI instruments have a limited lifetime, data from different instruments have been 'daisy-chained' together to estimate the long-term variation (now covering more than three solar cycles), which requires inter-calibrating the instruments using intervals when both were in operation. Historically, there have been three main data composites that have been in widespread use: (i) TSI$_{PMOD}$, generated and maintained at Physikalisch-Meteorologisches Observatorium Davos, PMOD [10]; (ii) TSI$_{RMIB}$, produced at the Royal Meteorological Institute of Belgium, RMIB [11]; and (iii) TSI$_{ACRIM}$, generated using data from the series of three ACRIM instruments [12]. The composites are made using different combinations of data and using different techniques, and hence it is not surprising that there are differences between them. The most important difference between the PMOD and ACRIM composites arose from a disagreement on how best to employ data from the H–F Nimbus-7/ERB instrument, which was needed to fill the 'ACRIM gap' between the end of ACRIM-1 on Skylab and the launch of ACRIM-2 on UARS (Upper Atmospheric Research Satellite). In particular, the PMOD composite made a correction for a known pointing direction glitch of the Nimbus-7 spacecraft in 1989, whereas the ACRIM composite did not make such a correction and this caused the major difference between the two [13]. A study by Dudok de Wit *et al.* [14] shows that the divergence of simultaneous observations (in both variations and
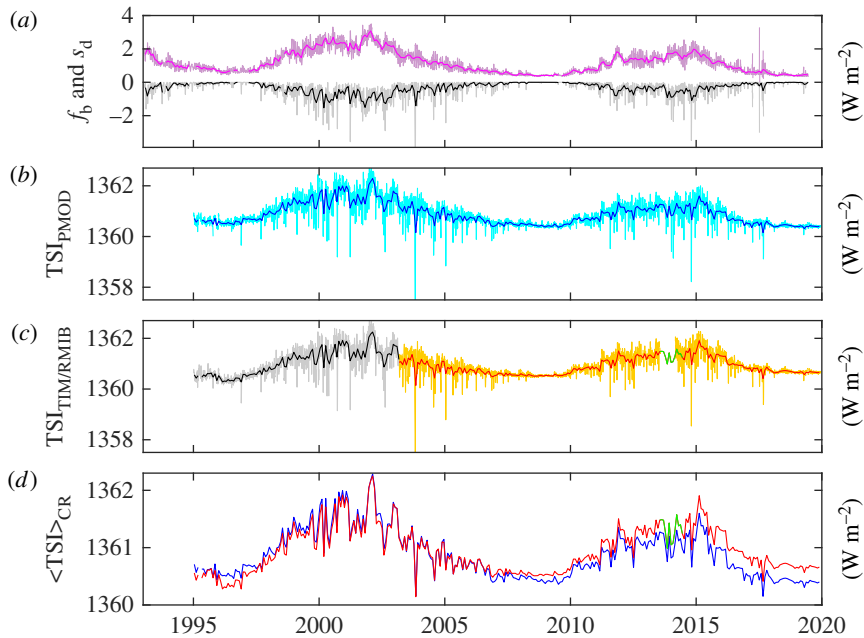
Figure 1. Total solar irradiance (TSI) variations after 1995. (*a*) The SATIRE (Spectral And Total Irradiance REconstructions) 'S' reconstructions of two contributions to TSI: the integrated facular brightening (f_b: daily values in pink and means over Carrington rotation (CR) intervals in mauve) and sunspot darkening (s_d: daily means in grey, CR means in black) [15]. (*b*) The PMOD (Physikalisch-Meteorologisches Observatorium Davos) composite of TSI observations (TSI$_{PMOD}$: daily means in cyan, CR means in blue) [10]. (*c*) The RMIB (Royal Meteorological Institute of Belgium) composite of TSI observations (TSI$_{PMOD}$: daily means in grey, CR means in black) [11] splined with data from the TIM (Total Irradiance Monitor) on the SORCE (SOlar Radiation and Climate Experiment) satellite (daily values in orange, CR means in red) [16]. The join of the spline is the start of the TIM data on 25 February 2003 and made by re-calibrating the RMIB data using a constant offset quantified using the mean values of the two datasets over the first year of TIM observations. The CR means in green are PMOD data with the best-fit offset of 0.23 W m^{-2} used to fill in a gap in the SORCE data. (*d*) Comparison of CR means of two observation series: PMOD composite (in blue) and the RMIB/TIM spline (in red). (Online version in colour.)

absolute levels) has decreased over time with the standard deviation decreasing in discrete steps around 1992 and 1996.

We here use data from 1995 onwards when the agreement between simultaneous observations is considerably improved [14]. The start date was chosen to give two full solar cycles (and a full 22 year Hale solar magnetic cycle) in most datasets. Figure 1 shows variations over this interval for which the PMOD composite mainly comes from the VIRGO (Variability of Solar Irradiance and Gravity Oscillations), which is a combination of instruments on the SoHO (Solar and Heliospheric Observatory) spacecraft, with small data gaps filled in using ACRIM-2 data. The ACRIM composite comes from the ACRIM-2 and ACRIM-3 instruments and the RMIB composite comes from the DIARAD (DIfferential Absolute RADiometer) instrument on SoHO and SOVIM (SOlar Variable and Irradiance Monitor) on Eureca-1. In addition, TSI data in this interval have been obtained from TIM (Total Irradiance Monitor) on the SORCE (SOlar Radiation and Climate Experiment) satellite [16], from TCTE (Total Solar Irradiance Calibration Transfer Experiment), which operated from November 2013 until June 2019 on board the US Air Force Space Test Program spacecraft STPSat-3, and from the PREMOS (PREcision MOnitor Sensor) [9] and SOVAP instruments [17] on the Picard satellite. In addition, a new data composite, the Community Composite (v. 1, termed CCv01), has been developed which uses maximum-likelihood techniques to give the variation of the best estimate and its uncertainty over time [14].

(b) Total solar irradiance models

Recent research has shown the extent to which, and how, magnetic field structures threading the photosphere and lower solar atmosphere modify the solar photospheric emissions and hence the TSI (e.g. [11,15,18–20]). The basic concept for spectral irradiance (as a function of time t and wavelength λ) is encapsulated in

$$dI(\lambda, t) = \left(\frac{R_\odot^2}{R_1^2} \right) I_O(\lambda, t) \int_{\mu=0}^1 \left[L_D(\mu, \lambda, t) \left\{ 1 + \sum_M \alpha M(\mu, t) C_M(\mu, \lambda, t) \right\} \right] \mu \, d\mu, \qquad (1.1)$$

and the TSI is the integral of the spectral irradiance $dI(\lambda, t)$ over all wavelengths, λ. The integral in equation (1.1) is over the whole disc of the Sun, μ being the cosine of the angle subtended by the surface pixel in question and the centre of the visible disc and $L_D(\mu, \lambda, t)$ being the limb-darkening factor at a given wavelength. The sum is over all classes of magnetic features on the solar surface considered, M (e.g. sunspot umbrae, sunspot penumbrae, active region faculae, network faculae, ephemeral flux), which have pixel filling-factors α_M and contrast with respect to the quiet Sun of C_M (here defined as the ratio of the emission from the region of the magnetic feature of class M to the quiet-Sun emission for the same location on the disc, μ) (e.g. [21]). Any features not included in the set M are, by default, part of the quiet-Sun emission. $R_\odot$ is the mean radius of the visible solar disc and R_1 is the mean Sun–Earth distance.

In the absence of magnetic features ($\alpha_M(\mu, t) = 0$), equation (1.1) yields the quiet-Sun spectral irradiance $dQ(\lambda, t)$, which gives the quiet-Sun TSI, Q, when integrated over all wavelengths. Both dQ and Q are often taken to be constant for lack of knowledge of their true variability; however, because the limb-darkening function L_D, the quiet-Sun intensity I_O and the mean solar radius $R_\odot$ are all, in general, functions of time, this remains an assumption. Similarly, the contrasts for a given class of surface magnetic field C_M are generally assumed to be invariant with time.

If we group together terms such that

$$k_M(\mu, \lambda, t) = \left(\frac{R_\odot^2}{R_1^2} \right) I_O(\lambda, t) L_D(\mu, \lambda, t) a_M(\mu, t) C_M(\mu, \lambda, t), \qquad (1.2)$$

we get

$$dI(\lambda, t) = dQ(\lambda, t) + \int_{\mu=0}^1 \left[\sum_M k_M \right] \mu \, d\mu, \qquad (1.3)$$

and integrating over all wavelengths

$$\text{TSI}(t) = Q(t) + \sum_M \Delta\text{TSI}_M(t). \qquad (1.4)$$

The simplest groupings of magnetic phenomena are to combine sunspot umbra and penumbra into an average effect for which $\Delta\text{TSI}_M(t) = -s_d$, the sunspot-darkening factor, and similarly combine active region and network faculae into $\Delta\text{TSI}_M(t) = f_b$, the facular brightening, in which case

$$\text{TSI}(t) = Q(t) + f_b(t) - s_d(t). \qquad (1.5)$$

Figure 1a shows the variations in daily means and averages over solar Carrington rotation (CR) intervals of f_b and s_d computed using the SATIRE-S model from an equation equivalent to (1.1). For the interval covered by figure 1, these modelled values of s_d and f_b are based on full-disc 'white' light images and solar magnetograms (used to define the distribution across the visible disc of each class of magnetic structure, M) from three different magnetographs: for 1995–1999, data from the ground-based Kitt Peak Vacuum Telescope (KPVT) are used; for 1999–2009, data from the Michelson Doppler Imager (MDI) on the SoHO spacecraft; and for 2010–2019, the Helioseismic and Magnetic Imager (HMI) on the Solar Dynamics Observatory (SDO) spacecraft are used to construct SATIRE-S [15].

The above equations for modelling the TSI variation have been used in various ways. The most satisfactory modelling to date is the SATIRE-3D [22], in that it requires no calibration or

5

royalsocietypublishing.org/journal/rspa Proc. R. Soc. A 476: 2020077

fit parameter (other than the zero-level offset of instrumental data) to derive the TSI variability. This is achieved using three-dimensional (3D) MHD numerical simulations of the solar surface and atmosphere coupled with magnetograms from SDO/HMI. The modelled TSI variation is extremely similar to the SORCE/TIM observations and shows that the observed/modelled magnetic structures explain 95% of TSI variability. Unfortunately, SATIRE-3D is only available for April 2010 to July 2016, which is a short interval compared with the full 24 years studied here.

The next most satisfactory and physics-based model is SATIRE-S [15], being based on magnetograph data with the use of just one free fit parameter (the pixel filling-factor for faculae, α_f). The wavelength-integrated (bolometric) radiation values of the quiet Sun, faculae and sunspots (and hence the contrasts field C_M) at various μ are calculated on the basis of one-dimensional model atmospheres with a radiative transfer code from magnetograph data. From sunspot data and a photospheric magnetic flux transport model, synthetic solar magnetograph data can be generated and these were used to generate the SATIRE-T2 irradiance reconstruction that extends back to close to the start of telescopic observations of sunspots [23,24].

The next level in modelling complexity makes more extensive use of empirical fitting to the TSI data, and is consequently less independent of the TSI observations. The two main models in this category used here are EMPIRE (EMPirical Irradiance REconstruction [19]) and NRLTSIv2 (Naval Research Labs TSI v. 2 [20]). These are based on the 'proxy approach' using equation (1.5). The variabilities of the factors $f_b(t)$ and $s_d(t)$ are given by the linear combination of facular and sunspot indices, the coefficients of which are determined by multiple regression to measured TSI. The NRLTSIv2 coefficients are obtained by multiple linear regression whereas EMPIRE employs a weighted 'error-in-variables' linear regression scheme which avoids some problems associated with ordinary least-squares regression for which erroneous and uncertain data points have equal weight with lower-error data points. Because the proxy indicators used extend back to before the start of magnetograph data, these can be used to reconstruct irradiance variations back to the start of telescopic solar observations in the seventeenth century, as, for example, done in the NRLTSIv2 [20] and SATIRE-T [25] historic TSI variation reconstructions.

(c) Long-term variations of the quiet Sun

With the aforementioned generalized formulation to represent solar irradiance changes, one can estimate the change in irradiance between present-day magnetic activity levels and those during the last grand solar minimum, the Maunder minimum in the second half of the seventeenth century when sunspots were rare or completely absent [26,27]. Decreased TSI during the solar Maunder minimum is often invoked as the cause of an interval when the frequency of cold winters in Europe increased and palaeoclimate indicators show reduced average Northern Hemisphere temperatures, referred to as the 'little ice age' (a name that implies a much greater climate perturbation than it actually was; see [28]). However, close inspection shows that common features between the solar and terrestrial climate time series are small and not statistically significant [3]. In the absence of quiet-Sun changes, estimates of solar irradiance change between approximately 1700 (the end of the Maunder minimum) and 2019 (close to the solar cycle minimum at the end of solar cycle 24) of, for example, between 0.14 and 0.26 W m^{-2} for the SATIRE-T/S and -T2 reconstructions and 0.55 W m^{-2} for NRLTSIv2.

It has been pointed out that because the TSI models do not contain any allowance for changes in the quiet-Sun component, taking the difference between the models and the observations can provide evidence of long-term changes in the quiet-Sun component [29]. Some journal papers have postulated quiet-Sun variations to generate TSI reconstructions that have much larger long-term variations (e.g. [4,5]) than others that assume the quiet Sun to be constant, such as SATIRE-T/S [25], SATIRE-T2 [23,24] and NRLTSIv2 [20]. The resulting TSI reconstructions are contrasted in figure 2. The Egorova *et al.* [5] (hereafter *EEA18*) and Shapiro *et al.* [4] (hereafter *SEA11*) reconstructions are based on the postulate that there are weak, small-scale magnetic features (that have not yet been detected), which generate brighter quiet-Sun emissions (that have also not yet been detected). Both *SEA11* and *EEA18* present alternative reconstructions
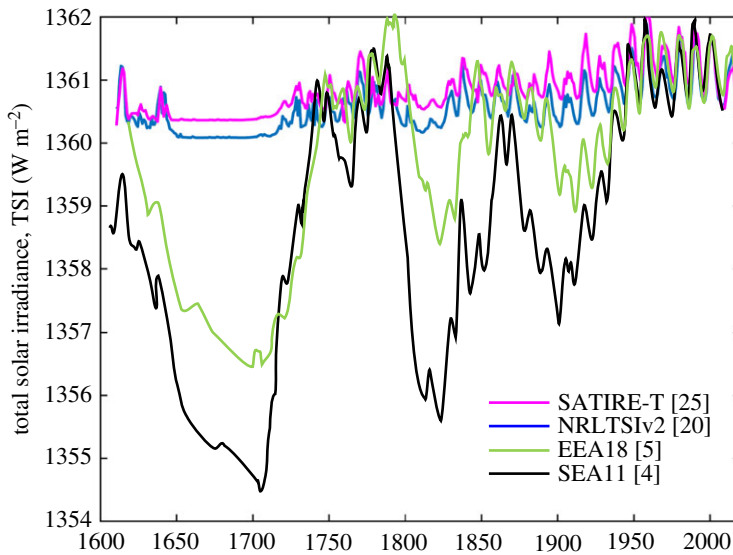
Figure 2. Model reconstructions of TSI since 1600. The *SEA11* reconstruction shown is that based on ^{10}Be abundances from South Pole ice cores [30] and the *EEA18* reconstruction is that based on a combination of various ^{10}Be and ^{14}C abundance records (referred to as PHI-US16 [31]). See text for details of other reconstructions. (Online version in colour.)

based on different heliospheric modulation potential variations derived from cosmogenic isotope abundance records. Figure 2 presents the *SEA11* reconstruction based on ^{10}Be abundances from South Pole ice cores [30] and the *EEA18* reconstruction shown is based on a combination of various ^{10}Be and ^{14}C abundance records (referred to as PHI-US16 [31]). The magnetic flux causing the proposed quiet-Sun irradiance changes is postulated to be residual and dispersed vestiges of sunspot and facular magnetic flux and can be quantized by the open solar magnetic flux (and hence heliospheric modulation potential) over a long prior interval. *EEA18* revised the TSI reconstructions of *SEA11*, mainly to take account of the comments made by Judge *et al.* [32]. We quantify the drift of the TSI between the end of the Maunder minimum (*ca* 1650–1710) and the present solar cycle minimum (at the end of 2019) with ΔQ_{MM} defined by

$$\Delta Q_{MM} = Q_{2019} - Q_{MM}. \tag{1.6}$$

The TSI reconstruction by *EEA18* shown in figure 2 gives $\Delta Q_{MM} = 4.13\,\mathrm{W\,m^{-2}}$, which is 68% of the $\Delta Q_{MM} = 6.05\,\mathrm{W\,m^{-2}}$ for the *SEA11* reconstruction shown. However, this is still 7.5 times larger than ΔQ_{MM} for the NRLTSIv2 reconstruction ($0.55\,\mathrm{W\,m^{-2}}$) and 27 times larger than ΔQ_{MM} for the SATIRE-T/S reconstruction ($0.14\,\mathrm{W\,m^{-2}}$).

As discussed above, the key difference between the *EEA18* reconstruction and others is that it attempts to include a long-term variation in the quiet-Sun contribution to TSI, Q. *EEA18* make their reconstruction by assuming that Q varies with the heliospheric modulation potential, Φ, which can be estimated from observations of galactic cosmic rays and the abundances of the cosmogenic isotopes that they generate, which are deposited and stored in terrestrial reservoirs. Although there is undoubtedly a link between Φ and TSI [33], a link with Q remains a conjecture.

The argument employed by *EEA18* and *SEA11* that there is a link between Φ and the quiet-Sun contribution to TSI, Q, can be summarized as follows. The key difference between dark sunspots and bright faculae is the dimension of the magnetic flux tube threading the photosphere (see the review by Lockwood [34]). In the case of sunspots, the reduction in upward energy flux to the surface caused by the inhibition of heat convection by the magnetic field causes a drop in the solar surface temperature from of order 6000 K to of order 4000 K and hence lower surface emission. On the other hand, for the much smaller magnetic flux tubes of faculae, the temperature at a

given level in the photosphere is kept high by radiation from the walls of the tube, but the raised magnetic pressure means that the particle density is reduced and optical depth increased inside the tube. This means we can see deeper into the photosphere where the temperature is a little higher and detect the 'bright walls' of the tube, especially when viewed from lower elevations (i.e. nearer the limb of the solar disc at lower μ). The effective temperature in faculae is raised over that of the quiet Sun by only about 100 K, but they are significant because there are very numerous. We know that the magnetic flux tubes in active regions that are initially large enough to be dark compared with the quiet Sun (i.e. sunspots) subsequently disperse into smaller flux tubes over a wider area (and so become bright faculae) on time scales of several days (e.g. [34]). *EEA18* and *SEA11* postulate that this process continues very slowly (on time scales of years to decades) such that very small flux tubes (that are well below the detection threshold set by spatial resolution and sensitivity of current magnetograph instruments) generate very small (in spatial dimensions and amplitude) enhancements in quiet-Sun irradiance, which are again below detection thresholds, but nevertheless add up to a significant contribution because they are so many in number. This means that, years after high sunspot activity, the quiet-Sun irradiance, Q, could be enhanced. The question then arises why such an effect on Q might be quantified by the heliospheric modulation potential Φ deduced from cosmogenic isotopes. The answer lies in the open flux of the Sun, F_S. Lockwood *et al.* [35] used historic geomagnetic activity data to show there were long-term variations in F_S which Solanki *et al.* [36] explained in terms of a continuity equation, where the F_S source term is related to the emergence of new magnetic flux tubes through the photosphere in active (sunspot) regions. The long loss time constants deduced by fitting the continuity equation to the data mean that F_S evolves over a number of years after the causal sunspot activity, in a manner that has some relation to the proposed variation in Q (the latter caused by the dispersal of those surface flux tubes). The relationship with Φ arises because it is the open solar flux (OSF) that shields Earth from galactic cosmic rays and so there is a strong relationship between Φ and F_S [30,37–39]. Much of this logical chain has been used with great success in the SATIRE TSI reconstructions and in using cosmogenic isotopes to deduce TSI variations throughout the Holocene [40]: the new element that *EEA18* and *SEA11* introduce is the postulate that the dispersal of active region flux continues over much longer time scales, giving a long-term variation in Q.

Consequently, *EEA18* and *SEA11* assume that the appropriate value of Φ is the average over the prior τ years, $\langle\Phi\rangle_\tau$, using a value for τ of 22 years (a full Hale polarity cycle in the solar magnetic field). This value for τ is imposed on *EEA18* and *SEA11* because they wish to use cosmogenic isotope data that have been smoothed over this time scale, but that does not mean that the results obtained are insensitive to the value adopted for τ. In this paper, we investigate the effects of different values of τ.

2. Stability of total solar irradiance observations

In order to detect a long-term variation in Q, we need the TSI observation stability to be good enough to make the error caused by long-term calibration drifts small. Ball *et al.* [9] took advantage of a switching of roles of the primary TSI radiometer on the PICARD mission (PREMOS-A) with the back-up radiometer (PREMOS-B) to test the fundamental hypothesis of self-calibrating two-radiometer experiments in space (i.e. that the sensitivity changes of the two instruments due to the space environment are identical for the same instrument type as a function of the integrated time that the instrument(s) are exposed to solar radiation). The results were applied to evaluate the stability of SORCE/TIM and SOHO/VIRGO TSI measurements, the latter being the basis for the PMOD composite in the interval under study here and derived by combining the data from both the PM06 and DIARAD instruments on the SoHO spacecraft. Ball *et al.* found that that PREMOS-B supported the SORCE/TIM TSI time evolution very closely (N.B. as did the fully independent SATIRE-3D model reconstruction, discussed in §1a, whereas more empirically based models had tended to support the PMOD composite that had been used to derive and tune the models [41]). Kopp [42] found that the drift in the PREMOS data was smaller

than that for TIM but by only 5.2 ppm yr^{-1} (note that parts per million per year, ppm yr^{-1}, is often used as a suitable measure quantifying the stability of irradiance instruments). From the uncertainties, these authors concluded that it is currently not possible to assess centennial time-scale changes in solar irradiance based on any of the presently existing TSI composites. *EEA18* concede this point and that the value of the ratio $\Delta Q / \Delta \langle \Phi \rangle_\tau$ that they employ (which they agree is critical to the long-term drift of their TSI reconstruction) is small compared with the observational noise.

Figure 3 studies the relative drift of various long-term TSI datasets. The figure uses PMOD as the comparison standard and plots the evolution of the differences in CR means from a data source X and the PMOD composite, $\Delta TSI = \langle TSI_X \rangle_{CR} - \langle TSI_{PMOD} \rangle_{CR} - O_{X,95}$, where $O_{X,95}$ is the zero-level offset that makes ΔTSI zero for CR number 1891, which approximately the first 27 days of 1995. Note that, in many cases, $\langle TSI_X \rangle_{CR}$ is not available for CR number 1891 and $O_{X,95}$ is computed by extrapolating $\langle TSI_X \rangle_{CR} - \langle TSI_{PMOD} \rangle_{CR}$ back linearly in time to this CR. Most of the variations show approximately linear trends, with ΔTSI revealing near constant drifts; the exception is the Community Composite, v. 1 CCv01 [14], shown by the yellow circles. If we take the whole interval 1995–2019, there is very little average drift between the PMOD and CCv1 composites; however, the plot reveals that this is somewhat misleading. There is a large decrease in ΔTSI for CCv1 over a 2 year interval starting midway through the year 2000 and, if we take CCv1 data for after decimal year 2003.5 only, the trend in ΔTSI is very similar in slope to that for the RMIB composite (mauve circles), which is based on data from the DIARAD instrument on SoHO. The drift for the DIARAD/RMIB instrument relative to the PMOD composite (which at this time comes from the VIRGO experiment, i.e. combining the data from both the PM06 and DIARAD instruments on SoHO) is linear and averages +0.0136 W m^{-2} yr^{-1} (+10.00 ppm yr^{-1}). The TIM instrument on SORCE also shows a highly linear drift with respect to PMOD, averaging +0.0261 W m^{-2} yr^{-1} (+19.21 ppm yr^{-1}) and, from the analysis of Kopp [42], this yields a linear drift for PREMOS of +0.0191 W m^{-2} yr^{-1} (+14.01 ppm yr^{-1}) over the relatively short interval for which it operated (27 July 2010–31 March 2013: note that the data are not shown in figure 3, but the drift inferred from Kopp [42] is given by the black dashed line). The green diamonds are for data from TCTE (Total Solar Irradiance Calibration Transfer Experiment) for November 2013 until June 2019: this yields a drift relative to PMOD of +0.0064 W m^{-2} yr^{-1} (+4.71 ppm yr^{-1}). The mauve inverted triangles are for SOVAP (SOlar VAriability Picard) on the Picard satellite [17]: these data are more scattered, but the average drift is +0.0135 W m^{-2} yr^{-1} (+9.91 ppm yr^{-1}). Given that all these data show a positive drift, it is most likely that the VIRGO data (as implemented in the PMOD composite) contain a false downward drift but we cannot state that as a certainty. The only instrument giving a downward drift relative to PMOD is ACRIM-3, for which the average drift is −0.0255 W m^{-2} yr^{-1} (−18.75 ppm yr^{-1}).

To put these calibration drifts into context, the *EEA18* reconstruction in figure 2 gives an estimate that the quiet-Sun TSI, Q, was lower in the Maunder minimum than in the current minimum by $\Delta Q_{MM} = 4.13$ W m^{-2}. (From other model and cosmogenic isotope data combinations, *EEA18* estimate that the range of ΔQ_{MM} is between 3.7 and 4.5 W m^{-2}.) This is a ΔQ_{MM} value of 4.13 W m^{-2} and corresponds to an average drift rate of −0.0129 W m^{-2} yr^{-1} (−9.51 ppm yr^{-1}) over the 269 years between 2009 and the end of the Maunder minimum in 1750. Hence, the drift rates in Q derived by *EEA18* were roughly one-quarter of the spread of uncertainties in the TSI data, which are in the measured range of ± 19 ppm yr^{-1}. Figure 3 shows that if we ignore the ACRIM-3 data as an outlier we roughly halve the measured TSI stability uncertainty to ± 10 ppm yr^{-1}, which is roughly equal to the drift rate proposed by *EEA18*. Note also that, in order to derive Q, we need to subtract from the observed TSI variation the modelled effects of magnetic features (such as using f_b and s_d estimates) and there are uncertainties in addition to TSI stability errors that are introduced by the computation of these model values.

3. The use of heliospheric modulation potential, Φ

The heliospheric modulation potential, Φ, is a quantitative measure of how the flux of galactic cosmic rays reaching Earth is reduced by the shielding effect of the OSF that emerges from the
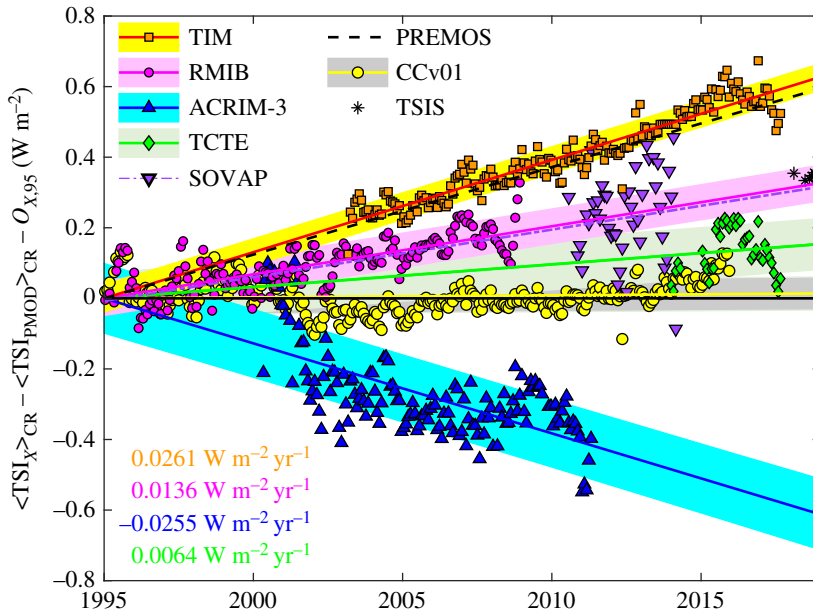
Figure 3. Analysis of the relative drifts in TSI observation series. All data are means over CR intervals and the difference between a given series (generic total solar irradiance TSI$_X$) and the PMOD composite, TSI$_{PMOD}$, is plotted as a function of date: $O_{X,95}$ is the zero-level offset for the TSI$_X$ series that makes the linear variation fitted to the TSI$_X$ data equal to that for TSI$_{PMOD}$ on 1 January 1995. The orange squares are for the TIM data; the mauve circles are RMIB composite; the blue triangles are for data from the ACRIM-3 (Active Cavity Radiometer Irradiance Monitor) instrument on the ACRIMSAT spacecraft [12] and the green diamonds are for data from TCTE (Total Solar Irradiance Calibration Transfer Experiment), which operated from November 2013 until June 2019. The yellow circles are for the Community Composite, v. 1 (CCv01 [14]). The coloured lines are the best-fit linear variations to the data points and are surrounded by paler-shaded areas giving the $2 - \sigma$ uncertainty in that linear regression (see key). The rates of drift for these instruments compared with the PMOD composite are given in the bottom left of the plot. The plot also shows data points and best-fit linear regression for SOVAP (SOlar VAriability Picard) on the Picard satellite [17] as purple inverted triangles and a purple dot-dash line. The 2 years of data from the TSIS-1 (Total and Solar Irradiance Sensor) satellite are shown as stars. The black dashed line is for the PREMOS (PREcision MOnitor Sensor) instrument on Picard (operated for 2010–2013) from the analysis of Kopp [42,43]. (Online version in colour.)

solar atmosphere and fills the heliosphere. The energy spectrum of galactic cosmic rays at the Earth's orbit is often described using the so-called force-field approximation and the modulation potential is the only time-varying factor in that description. Usoskin *et al*. [44] reconstructed the variation of the heliospheric modulation potential using the model of the OSF since the Maunder minimum of Solanki *et al*. [36]. This OSF reconstruction is based on sunspot observations and tuned using the OSF variation derived from geomagnetic data from 1868 onwards by Lockwood *et al*. [35] and Lockwood [37]—reconstructions that have been verified using multiple sources and extended back to 1844 by Lockwood *et al*. [45]. The reconstruction of Φ has been extended in figure 4 to the end of 2019 and agrees well with the OSF and near-Earth magnetic field observed from spacecraft and with the heliospheric modulation potential derived from neutron monitor data for after 1955 and from cosmogenic isotopes before then [39,47,48].

The reconstructed heliospheric modulation parameter Φ since the end of the Maunder minimum is shown by the black line in figure 4*a*. Note that this rises much more steeply at the end of the Maunder minimum than does the sunspot number—this is caused by the rapid increase in OSF F_S at this time because loss rates in F_S are low (because F_S is low), as shown by numerical modelling of F_S using continuity equations [36,49]. This points to a likely limitation in using Φ as a proxy for Q at this time because the sunspots that are postulated to be the source in the subsequent rise in Q do not rise as rapidly. Hence, there may be nonlinearities that
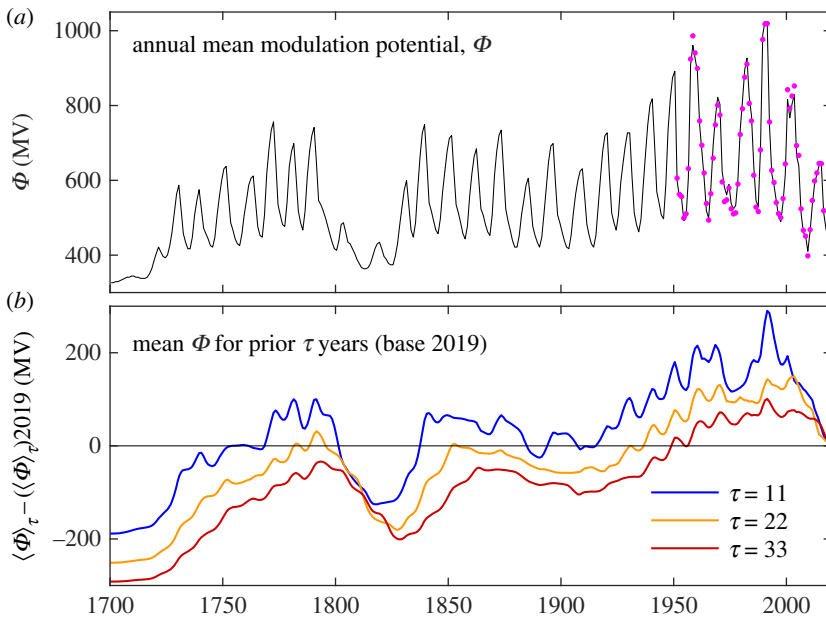
Figure 4. (a) The variation in the heliospheric modulation parameter, Φ. The mauve dots are annual means from the analysis of data from neutron monitors, calibrated using direct measurements of the cosmic ray spectrum performed by the Payload for Antimatter Matter Exploration and Light-nuclei Astrophysics (PAMELA) space-borne spectrometer [46]. The black line is a second-order polynomial fit of the reconstruction of Usoskin et al. [44] based on cosmogenic isotope data and modelling using the open solar flux since 1868 derived from geomagnetic data by Lockwood et al. [35]. This has been extended to 2019 using a linear regression spline of observed counts from neutron monitors. (b) Running means of the Φ values shown in (a), $\langle \Phi \rangle_\tau$, over the interval of duration τ years prior to the time in question. These are shown as an anomaly relative to the value of $\langle \Phi \rangle_\tau$ for 2019. Blue, orange and red lines are for τ of 11, 22 and 33 years, respectively. (Online version in colour.)

are not yet accounted for. The mauve dots in figure 4a are annual means from the analysis of data from a number of ground-based neutron monitors, calibrated using direct measurements of the cosmic ray spectrum performed by the Payload for Antimatter Matter Exploration and Light-nuclei Astrophysics (PAMELA) space-borne spectrometer [46].

Figure 4a shows that the solar cycle coming to an end at the time of writing (cycle 24) has been remarkably similar to cycle 14 (ca 1900–1911) and all solar and geomagnetic indicators indicate that, by the end of 2019, the Sun has returned to conditions that were last seen in about 1900. Between 1900 and 2019, the Sun has been through a grand activity maximum (here called the Modern Grand Solar Maximum; MGSM), which peaked in about 1985 [50,51]. Note that there has been some debate about the MGSM because it is more apparent in parameters that are related to integrated sunspot numbers, such as cosmogenic isotope abundance [52] and OSF [51], and less obvious in sunspot numbers themselves, which return to near zero at each sunspot cycle minimum [53]. Nevertheless, this maximum is clearly present in the sunspot data because sunspot cycle 24 (2009–present) has been of a similar small amplitude to cycle 14 (1901–1913), whereas cycle 19 (1954–1964) was the largest known and cycles 18, 21 and 22 were also large.

Figure 4b shows running means of the Φ values shown in figure 4a, $\langle \Phi \rangle_\tau$, where the mean is calculated for the number years indicated prior to the date to which it is attributed. These are shown as an anomaly relative to $\langle \Phi \rangle_\tau$ for 2019. Blue, orange and red lines are for $\tau = 11$, 22 and 33 years, respectively, which are used because they minimize the residual decadal-scale solar cycle variations in the data and so show the centennial-scale changes most clearly. (Note that the sunspot cycle varies in length between about 9 and 14 years and so its effects are not completely removed by this smoothing.) The adoption of $\tau = 22$ years (the average length of the
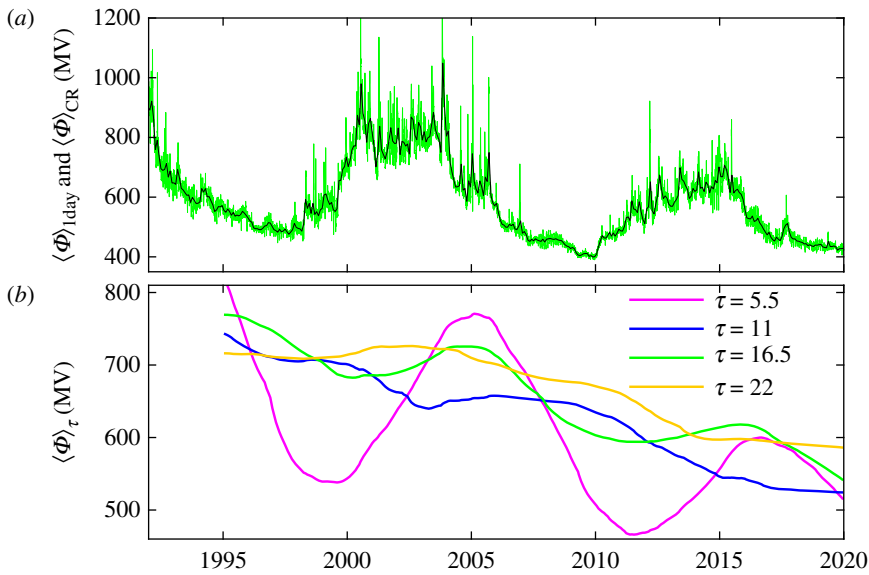
Figure 5. (a) The variation of modulation parameter Φ over 1995–2019: the green line shows daily means, $\langle\Phi\rangle_{1day}$, and the black line shows means over CR periods, $\langle\Phi\rangle_{CR}$. (b) Means of Φ over prior intervals of duration τ of 5.5 years (mauve line), 11 years (blue line), 16.5 years (green line) and 22 years (orange line). (Online version in colour.)

full Hale polarity cycle of the solar field) employed by *EEA18* to give a proxy variation of Q was chosen since the cosmogenic isotope data used to reconstruct the solar modulation potential used in Shapiro *et al.* [4] were provided with a resolution of 22 years. *EEA18* retained this averaging. However, figure 4b demonstrates that this averaging period *must* have had an effect on both the waveform and the amplitude of the reconstruction. The plot for $\tau = 11$ years (blue line) shows that the value of $\langle\Phi\rangle_\tau$ in 2019 (and hence the value of the quiet-Sun TSI) is very similar to the average for 1850–1900, meaning that any upward drift in $\langle\Phi\rangle_\tau$ between 1900 and 1985 is cancelled by the fall between 1985 and 2019. As discussed above, this rise and fall in solar magnetic activity and in Φ has been termed the MGSM [51] and the decline following the peak of the MGSM in about 1985 was noted by Lockwood & Frölich [50] and has continued up to the present day. If, on the other hand, $\tau = 22$ years is adopted (the orange line), the MGSM is still clearly defined but, because a larger interval of prior history is considered, the 2019 value is raised because of the prior MGSM, whereas the values for 1850–1900 are lowered because of the prior lower values during the Dalton minimum. Similarly, values at the end of the Maunder minimum are lowered by the prior low values. This effect is even more pronounced if $\tau = 33$ years (the red line) is adopted. Modern climate simulations are often concerned with the interval of global observations of the surface temperature (roughly 1850 to the present) and figure 4b shows that adoption of $\tau = 11$ years would mean that the use of $\langle\Phi\rangle_\tau$ as a proxy indicator for the quiet-Sun TSI, Q, would introduce no change between the late nineteenth century and today, whereas the value of $\tau = 22$ years does. Hence, the amplitude of the long-term drift in quiet-Sun irradiance depends critically on the choice made for the averaging time scale τ.

Note that, as well as the amplitude of the anomaly in $\langle\Phi\rangle_\tau$ (with respect to the present day, i.e. 2019) showing a dependence on τ, so does the timing of features such as the peak of the MGSM and the Dalton minimum. This is an inevitable consequence of taking the mean over the prior interval, which is central to the *SEA11* and *EEA18* formulation and rationale.

Figure 5 shows the detail of the effect on the $\langle\Phi\rangle_\tau$ anomaly (with respect to 2019) of averaging over the prior interval of duration τ for the interval covered by figures 1 and 3. Figure 5a shows the daily and CR means for 2019–2019 (inclusive) and figure 5b shows $\langle\Phi\rangle_\tau$ for various values of τ. The mauve line is for $\tau = 5.5$ years (half an average solar cycle period), for which a clear solar

cycle variation is still seen, but the peak is shifted into the declining phase of the sunspot cycle (remember we are averaging over the prior interval of duration τ). This solar cycle variation is largely supressed for $\tau = 11$ years (blue line), which yields an almost linear decline over the whole period. For $\tau = 16.5$ years (green line), the peaks in the declining phase of solar cycles return but are weaker, superposed on a decline that is very similar to that for $\tau = 11$ years. For $\tau = 22$ years (orange line), the decline in $\langle \Phi \rangle_\tau$ all occurs after about 2002, with a plateau at 1996–2002. Hence, the period 1995–2019, as well as providing higher stability TSI data and better agreement between the different radiometers, also gives a large downward drift in $\langle \Phi \rangle_\tau$, which opens up the possibility of quantifying the effects of $\langle \Phi \rangle_\tau$ variations on the quiet-Sun TSI, Q, and defining the factor $\Delta Q / \Delta \langle \Phi \rangle_\tau$.

4. The scaling factor relating Q and $\langle \Phi \rangle_\tau$

EEA18 note that the factor $\Delta Q / \Delta \langle \Phi \rangle_\tau$, used to scale $\langle \Phi \rangle_\tau$ to give Q, is critical to the TSI reconstruction, but also note that, as shown in §2, the drift in calibration of the TSI observations means that it cannot be determined with the required accuracy.

From equation (1.4), the variation of the quiet-Sun irradiance can be determined from the variation of the difference between the observed TSI_o and the value modelled from magnetic features in the solar surface, TSI_m. We have several data composites and a number of models we can employ for this. The uncertainty in Q will be a combination of the uncertainties in TSI_o and TSI_m.

(a) Total solar irradiance observations

Figure 3 shows the relative stability of the various TSI instruments that were discussed in §2. The various slopes of the plots for the different instruments can only tell us about their relative drifts and not the absolute drift. The PMOD composite sits almost exactly midway between the two extremes, which are the TIM data and the ACRIM-3 data: hence, we here can consider the uncertainty range in the drift of the PMOD composite to be between $+0.0261$ and $-0.0255\,W\,m^{-2}\,yr^{-1}$. The consensus between the more recent instruments (SOVAP, TCTE, TSIS and PREMOS) agrees best with the RMIB composite (suggesting that PMOD actually has a downward drift) and TIM and ACRIM-3 set an uncertainty range for the drift of RMIB of between $+0.0125$ and $-0.0391\,W\,m^{-2}\,yr^{-1}$. Because the drifts of RMIB and TIM are relatively similar, we make a composite of these two, splining them together with a zero-level offset which is the difference in the mean values for the TIM–RMIB overlap period of 2003–2009 and adjusting the RMIB data to agree with TIM. We take the average of the RMIB and TIM drifts for the RMIB/TIM composite, and use the TIM and ACRIM-3 data to set uncertainty limits of $+0.0063$ and $-0.0453\,W\,m^{-2}\,yr^{-1}$. We also use this uncertainty range for the TIM data but shifted upwards by the relative drift of TIM and RMIB, which is $+0.0125\,W\,m^{-2}\,yr^{-1}$. Note that the ACRIM-3 data are outliers compared with the other instruments and we here use them only to set extremes to the uncertainties.

(b) Total solar irradiance models

An important point to note about the models is that they have all been fitted to the data in some way. This is a problem because a multivariate fit can easily attribute a variation in the data to the wrong parameter (often referred to as 'overfitting'). In our study, this means that the quiet-Sun variation could be attributed to, for example, network faculae (and so underestimated) or could be increased because the fit is struggling to fit a different feature of the data. From this point of view, the ideal model for us to use is SATIRE-3D because it is not fitted to the observed variation at all. (It does use a zero-level offset to match the observations, but there are no fit parameters that alter the temporal variation.) Unfortunately, SATIRE-3D is only available for a limited interval (between decimal years 2010.3 and 2016.6). Figures 6 and 7 show the scatter plots of observed and
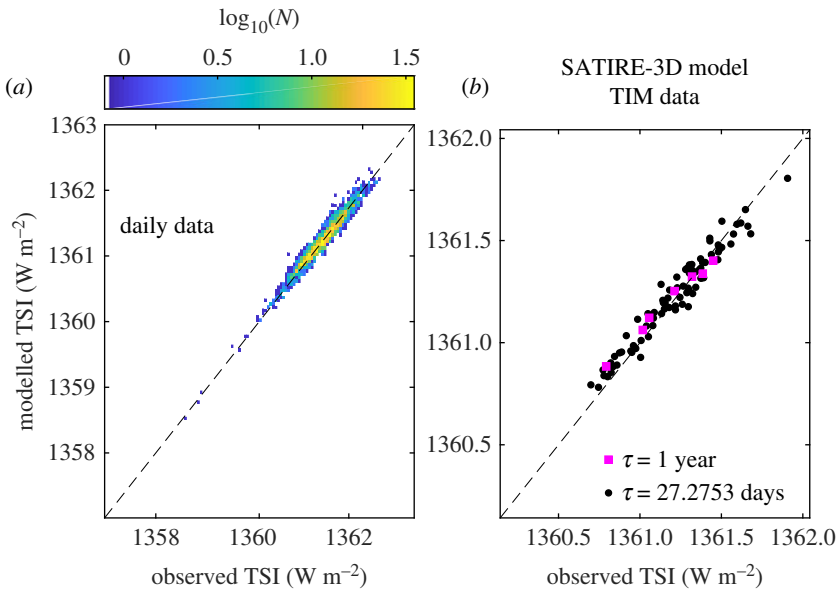
Figure 6. Scatter plots of the SATIRE-3D model results with the TIM observations. (*a*) The logarithms of the number of daily samples in bins are 0.05 W m^{-2} by 0.05 W m^{-2} in extent, colour-coded and plotted as a function of observed (TSI$_o$) and modelled (TSI$_m$) total solar irradiance. (*b*) Scatter plot of annual means of TSI$_m$ as a function of TSI$_o$ (mauve squares) and means over CR intervals (black dots). The dashed line shows TSI$_m$ = TSI$_o$. (Online version in colour.)
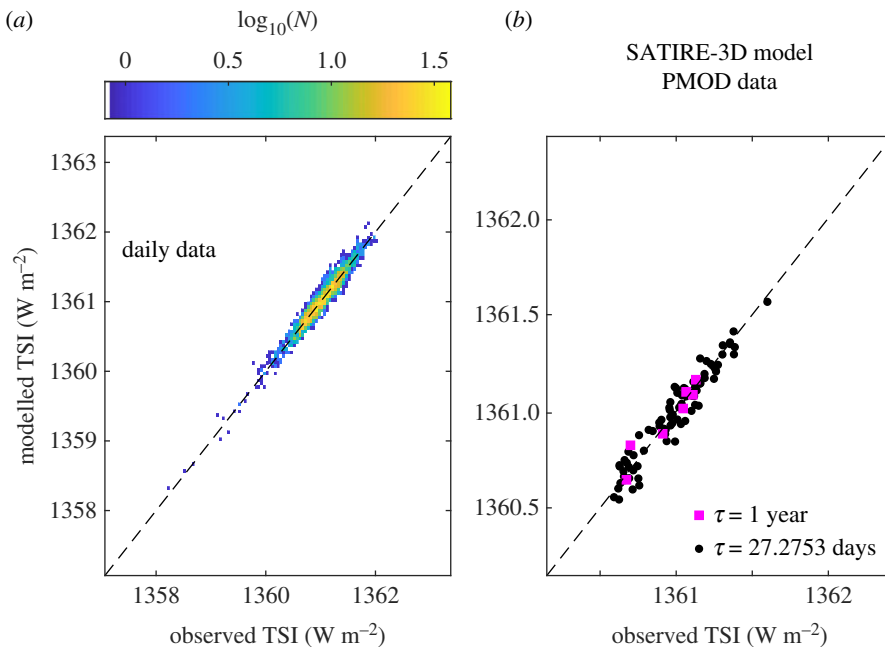

Figure 7. Scatter plots of the SATIRE-3D model results with the PMOD data composite in the same format as figure 6. (Online version in colour.)

SATIRE-3D modelled values (for daily values, means over CRs and means over calendar years): figure 6 is for the RMIB/TIM composite (but at this time all the data come from TIM) and figure 7 is for the PMOD composite. It can be seen that the agreement is excellent in both cases and that

Table 1. The levels of agreement between the modelled total solar irradiance values, TSI_m, and simultaneous observed values, TSI_o. The interval of data and model overlap is given in decimal years. The correlation coefficient r is given for daily, CR interval and annual means. In each case, the r.m.s. deviation, $\Delta_{rms} = \langle (TSI_o - TSI_m)^2 \rangle^{1/2}$, is given.

	data, TSI_o	model, TSI_m	interval (decimal years)	daily means		CR means		annual means	
				r	Δ_{rms} (W m^{-2})	r	Δ_{rms} (W m^{-2})	r	Δ_{rms} (W m^{-2})
a	RMIB/TIM	EMPIRE	1995.0–2017.4	0.936	0.190	0.961	0.131	0.960	0.119
b	PMOD	EMPIRE	1995.0–2017.4	0.945	0.200	0.971	0.150	0.972	0.144
c	TIM	EMPIRE	2003.2–2017.4	0.960	0.123	0.983	0.066	0.986	0.052
d	RMIB	EMPIRE	1995.0–2009.0	0.942	0.219	0.974	0.157	0.977	0.146
e	RMIB/TIM	SATIRE-S	1995.0–2019.5	0.910	0.203	0.900	0.179	0.883	0.173
f	PMOD	SATIRE-S	1995.0–2019.5	0.975	0.147	0.984	0.122	0.989	0.112
g	TIM	SATIRE-S	2003.2–2019.5	0.959	0.141	0.955	0.127	0.933	0.131
h	RMIB	SATIRE-S	1995.0–2009.0	0.946	0.232	0.961	0.199	0.960	0.192
i	RMIB/TIM	NRLTSIv2	1995.0–2019.0	0.938	0.181	0.960	0.126	0.958	0.117
j	PMOD	NRLTSIv2	1995.0–2019.0	0.948	0.201	0.970	0.158	0.971	0.150
k	TIM	NRLTSIv2	2003.2–2019.0	0.960	0.116	0.983	0.060	0.986	0.050
l	RMIB	NRLTSIv2	1995.0–2009.0	0.943	0.216	0.972	0.159	0.973	0.149
m	TIM	SATIRE-3D	2010.3–2016.6	0.975	0.086	0.975	0.063	0.995	0.054
n	PMOD	SATIRE-3D	2010.3–2016.6	0.972	0.090	0.962	0.063	0.953	0.055

the only difference is that the data points are not quite aligned in the same way to the slope of the dashed line in the two cases, reflecting the different instrumental drift of the two datasets.

The next most satisfactory reconstruction for our purposes is SATIRE-S, which is based on magnetograph data but has the one free parameter, the magnetogram pixel facular filling-factor. We also use the EMPIRE and NRLTSIv2 model reconstructions, which reproduce the data extremely well but we need always to bear in mind that they are based on multiple regression fits to the data. Employing more than one dataset or data composite with each model can help us identify an overfitting problem that may be influencing our estimates of the quiet-Sun irradiance variation.

(c) Combinations of data and models

Table 1 lists the combinations used in the present study: it gives the overlap period covered by both the model and data series in each case and also gives the correlations between TSI_o and TSI_m and root-mean-square (r.m.s.) deviations $\Delta_{rms} = \{ \langle (TSI_o - TSI_m)^2 \rangle \}^{1/2}$ for daily values and for means over CR intervals and calendar years. Figure 8 shows the derived variations in $Q = TSI_o - TSI_m$ for each of the 14 combinations listed in table 1. Note that figure 5b shows that $\langle \Phi \rangle_\tau$ has a net downward drift over the interval we study, although that drift is close to linear only at τ values that are close to multiples of the solar cycle length as then the solar cycle variation is largely averaged out. By contrast, figure 8 shows that Q can drift up or down or remain level for different data/model combinations. For example, the SATIRE-S and RMIB/TIM composite comparison (figure 8e) gives a clear upward drift in Q (the opposite to that in $\langle \Phi \rangle_\tau$), whereas the SATIRE-S and PMOD composite comparison (figure 8f) gives a level Q after a weak early rise and the EMPIRE/PMOD and NRLTSIv2/PMOD comparisons (figure 8b,j) show falls after an initial rise. Note that $\langle \Phi \rangle_\tau$ for $\tau = 22$ years shows a plateau followed by a fall (the orange line in figure 5b) and so similar behaviour in derived Q will correlate well. These results are not surprising, given

that the free parameter for SATIRE-S is determined using the PMO6 radiometer [15], which is the part of the VIRGO combination that is responsible for the long-term component of the VIRGO data and hence the post-1995 PMOD composite. The similarity between EMPIRE and NRLTSIv2 is because the construction is very similar except the former accounts for the noise in observations in the regression calculations [22]. It is worth noting that SATIRE-S and EMPIRE/NRLTSIv2 use different proxies to represent the magnetic/facular component driving the long-term changes, the photospheric magnetic field and the Mg-II index, respectively, and these have different temporal behaviours.

The comparisons with SATIRE-3D are particularly revealing: the SATIRE-3D/TIM comparison (figure 8m) gives an upward drift in Q, whereas the SATIRE-3D/PMOD comparison (figure 8n) gives a downward drift in Q. Given that SATIRE-3D is unique in not using a fit to the data variation, this indicates the key element in determining the polarity of the correlation between $\langle \Phi \rangle_\tau$ and Q is set by the stability drift of the instrument used.

5. Analysis procedure

Figures 9 and 10 show two examples of analysis of the correlation between the variations of Q (shown in figure 8) and the heliospheric modulation potential, averaged over the prior τ years $\langle \Phi \rangle_\tau$. These are important because they study the effect of averaging time scale τ and we need to carry out a sensitivity study for the averaging time scale τ because it is not set theoretically: the rationale for a link between Q and Φ is the hypothesis that facular flux tubes disperse into slightly brighter subvisual flux tubes, but we have no indication of the time scale that this might happen on. Figure 5b gives four examples of $\langle \Phi \rangle_\tau$ at four different values of τ, which are marked in figures 9 and 10 by vertical lines using the same colour scheme. Figure 9 is for Q derived from the difference between the RMIB/TIM data composite and the EMPIRE model, whereas figure 10 is for the RMIB data composite (without extension using TIM) and the SATIRE-S model. These examples are chosen to illustrate both general properties of the behaviour and some differences. Figures 9a and 10a show the correlation coefficient r between Q and $\langle \Phi \rangle_\tau$ as a function of τ and, in both cases, the peak correlation is an anti-correlation at τ near 11 years. In both cases, there is a secondary peak at τ near 22 years. Figures 9c and 10c show the statistical significance $S(\tau)$ of the difference between the peak $|r|$ (r_p, at $\tau = \tau_p$) and that for general τ, $r(\tau)$: $S(\tau)$ is evaluated using the Meng-Z test [54], which allows for the inter-correlation between the two time series evaluated, with allowance also made for the effect of autocorrelation of the time series [55]. The horizontal dashed and dot-dash lines are at $S = 1 - 0.68$ and $S = 1 - 0.95$ and so mark the $1 - \sigma$ and $2 - \sigma$ confidence levels of the difference between r_p and $r(\tau)$: between the dashed lines is where the difference between $|r_p|$ and $|r(\tau)|$ is not large enough to be significant at the $1 - \sigma$ level. In figure 9, the peak at $\tau \approx 22$ years is significantly lower (at the $1 - \sigma$ level) than that at $\tau \approx 11$ years, whereas in figure 10 it is not. In both the cases using the SATIRE-3D model, the peaks near 22 years and near 11 years are almost exactly the same. For all Q data series, the comparisons yield these two correlation peaks because the variations in Q are close to linear, something that is true for $\langle \Phi \rangle_\tau$ when we average over an integer number of complete solar cycles. Figures 9b and 10b show how the effect of τ on the best-fit regression influences the change in Q deduced between the end of the Maunder minimum and 2019, ΔQ_{MM}. As expected from figure 4b, that difference is larger for $\tau \approx 22$ years than for $\tau \approx 11$ years.

Because the difference in the correlations between $\tau = 22$ years and $\tau = 11$ years is not generally significant, we here look at both these values for τ. For each of these two values and each model–data comparison, we use the best-fit regression of $\langle \Phi \rangle_\tau$ and Q to reconstruct Q back to the Maunder minimum using the variation of $\langle \Phi \rangle_\tau$. To evaluate the uncertainty around this best-fit regression due to the uncertainty in the stability of the instruments, we use the maximum drifts derived in §4a from figure 3. These drifts are applied to the derived Q variation. In figures 11b,d and 12b,d, the mauve circles are a scatter plot of the simultaneous $\langle \Phi \rangle_\tau$ and Q values, for which the black line is the best-fit linear regression. From the variation of $\langle \Phi \rangle_\tau$ with time since the end of the Maunder minimum, this gives the reconstruction of Q shown in black in the corresponding plots
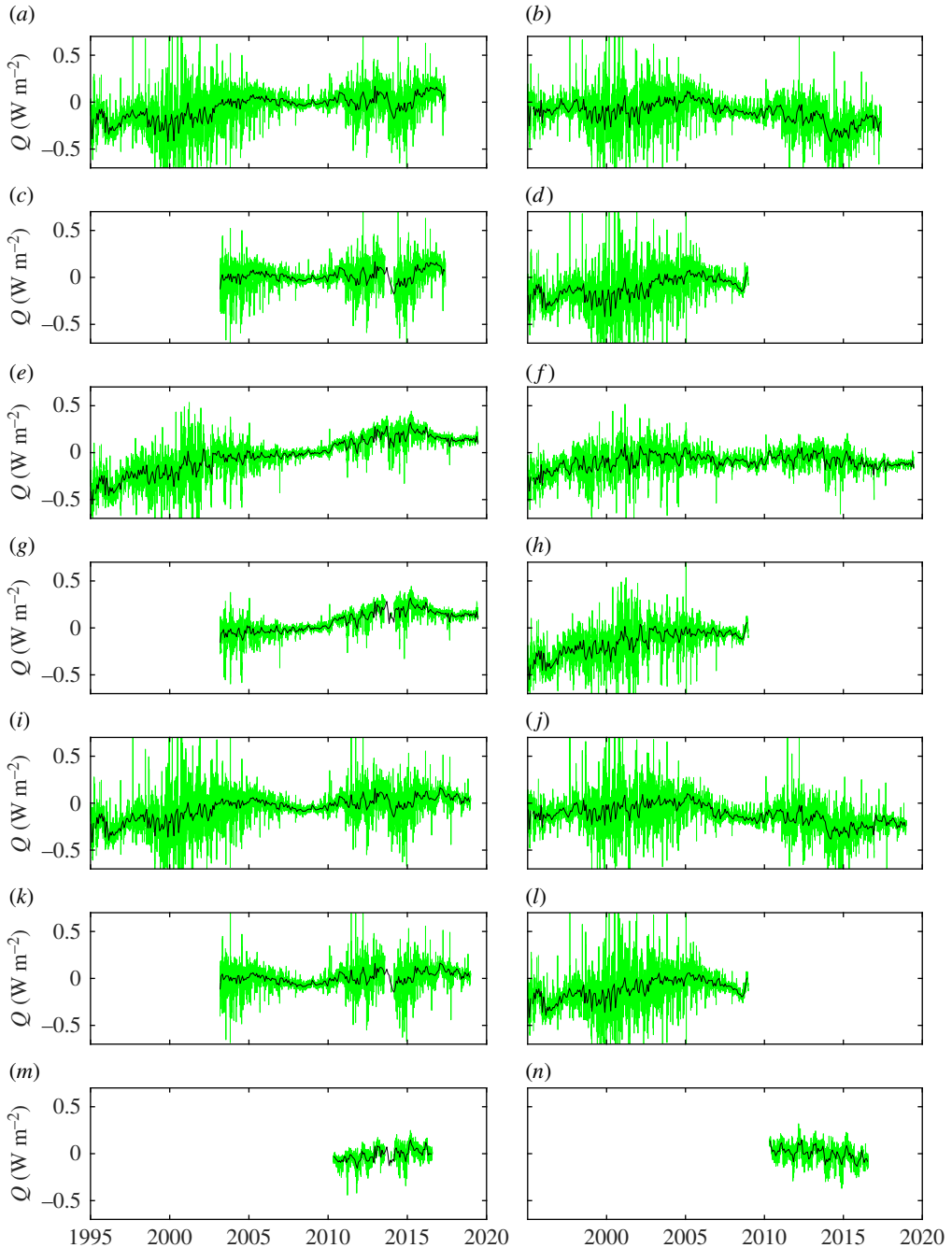
Figure 8. Variations of quiet-Sun irradiance, $Q = TSI_o - TSI_m$, for the 14 combinations of TSI_o and TSI_m used in this paper and listed in table 1. The green lines show daily values and the black lines are averages over solar CR periods (of duration approx. 27 days). (*a*) RMIB/TIM data, EMPIRE model; (*b*) PMOD data, EMPIRE model; (*c*) TIM data, EMPIRE model; (*d*) RMIB data, EMPIRE model; (*e*) RMIB/TIM data, SATIRE-S model; (*f*) PMOD data, SATIRE-S model; (*g*) TIM data, SATIRE-S model; (*h*) RMIB data, SATIRE-S model; (*i*) RMIB/TIM data, NRLTSIv2 model; (*j*) PMOD data, NRLTSIv2 model; (*k*) TIM data, NRLTSIv2 model; (*l*) RMIB data, NRLTSIv2 model; (*m*) TIM data, SATIRE-3D model; (*n*) PMOD data, SATIRE-3D model. (Online version in colour.)

in figures 11*a,c* and 12*a,c*. The cyan squares and yellow triangles show the same data points after application of the minimum and maximum upward drift estimates (deduced from the ACRIM-3 and TIM data, respectively). The blue and red lines (bounding the grey area) are the best-fit
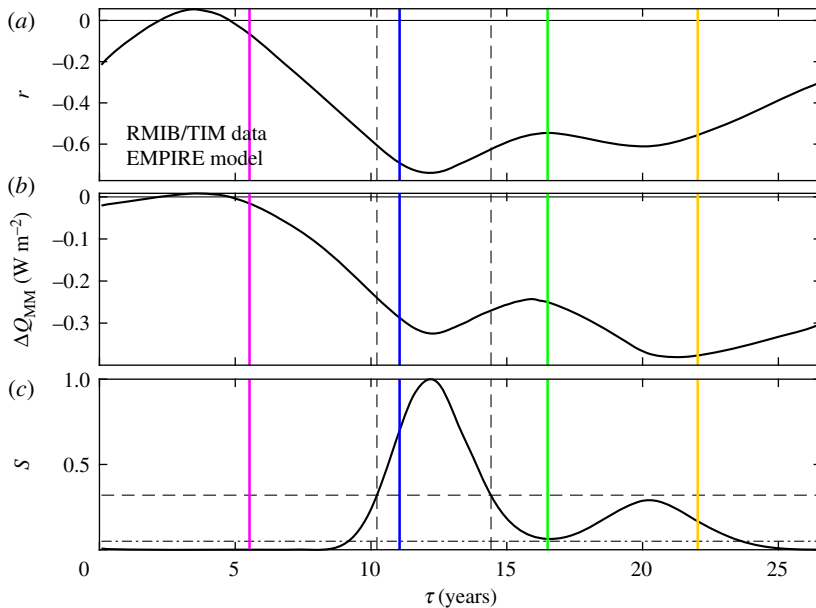
Figure 9. Analysis of the relationship of CR means of quiet-Sun irradiance Q, derived from the difference between the RMIB/TIM data composite and the EMPIRE model, and the heliospheric modulation potential averaged over the prior interval of duration τ, $\langle\Phi\rangle_\tau$. (a). The correlation coefficient r between Q and $\langle\Phi\rangle_\tau$ as a function of τ. (b) The difference between the Q values at the end of the Maunder minimum and for 2019 from the best-fit linear regression for the τ in question. (c) The significance $S(\tau)$ in the difference between the peak $|r|$ (r_p, at $\tau=\tau_p$) and that for general τ, $r(\tau)$, computed using the Meng-Z test. The horizontal dashed and dot-dash lines are at $S=1-0.68$ and $S=1-0.95$ and so mark the $1-\sigma$ and $2-\sigma$ levels. In all three panels, the mauve, blue, green and orange vertical lines are at τ of 5.5, 11, 16.5 and 22 years, respectively (the time variations shown in figure 4b). Between the dashed lines is where the difference between $|r_p|$ and $|r(\tau)|$ is not large enough to be significant at the $1-\sigma$ level. (Online version in colour.)

regression lines and these give limits to the uncertainty band (shaded grey) in the temporal reconstruction of Q.

Figure 13 is the ensemble of all 28 reconstructions of the kind illustrated in figures 11 and 12. These are for the 14 model–data combinations and $\tau=22$ years and $\tau=11$ years in each case. The cyan and orange lines are the mean and median of the ensemble, respectively. The grey area defines the range between the maximum and the minimum of the set of 28 cases for any one year. The ensemble members show two types of behaviour depending on the data used. The black lines are for the PMOD data composite and almost all show a maximum Q in the MGSM and minima in Q during the Dalton and Maunder minima. On the other hand, the mauve lines show the results for the TIM, RMIB and TIM/RMIB composite and almost all show the reverse behaviour with minimum Q during the MGSM and maxima in Q during the Dalton and Maunder minima. Two of the three exceptions to this rule are for the SATIRE-S/PMOD comparison, which shows almost zero Q in all years for $\tau=11$ years and very weakly contrary behaviour for $\tau=22$ years. This appears to be indicating that SATIRE-S, being tuned to PMOD, has accounted for the quiet-Sun variation using network faculae alone: this could be reproducing reality but could equally be an example of overfitting. The third exception is for the NRLTSIv2 model, the RMIB data and $\tau=22$ years (but not $\tau=11$ years), which shows contrary (PMOD-like) behaviour. In figure 13, the maximum and minimum of the uncertainty band in the MGSM—and the minima and maxima in the Dalton and Maunder minima— are always set by the ACRIM-3 and TIM data, respectively. Note that the largest deviations and variability in Q are found during the Maunder minimum (and to a lesser extent during the Dalton minimum) and during the peak of the MGSM. This is
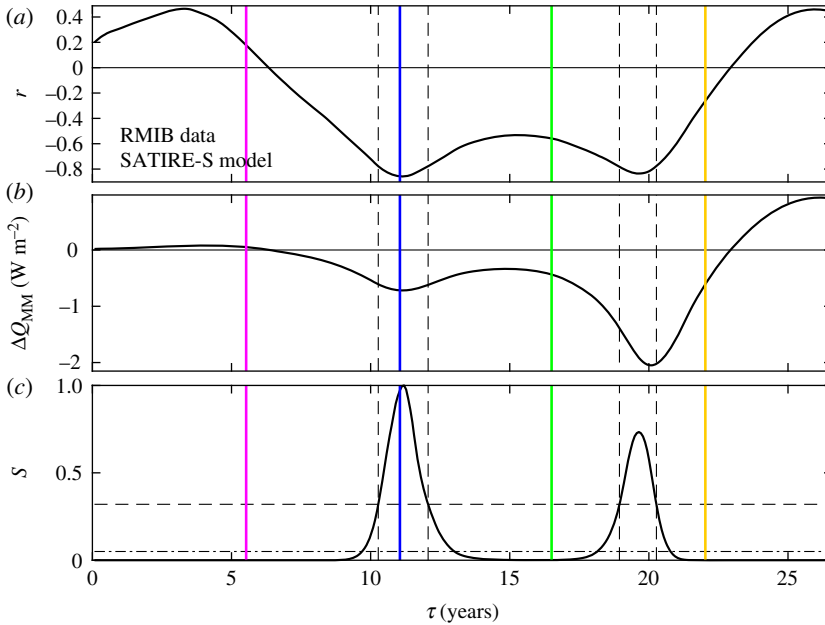
Figure 10. Analysis of the relationship of CR means of quiet-Sun irradiance Q, derived from the difference between the RMIB data composite and the SATIRE-S model, and the heliospheric modulation potential averaged over the prior interval of duration τ, $\langle \Phi \rangle_\tau$. The format is as for figure 9. (Online version in colour.)

because of the waveform of Φ shown in figure 4 and the fact that the $Q = 0$ values are defined for 2019, which is close to the minimum following the weak solar cycle 24, and the above intervals are when Φ deviates most from the value for 2019.

In figure 14, we add the variations in ΔQ derived in figure 13 to two reconstructions of TSI based on sunspot observations. These model reconstructions, TSI_m, employ the science of the effect of known photospheric magnetic features (sunspot umbrae and penumbrae, faculae). The NRLTSIv2 model [56] uses empirical relationships with sunspot numbers from modern TSI data to quantify the net effect. The SATIRE-T2 is a more physics-based reconstruction which simulates magnetograms from the sunspot observations using a model of magnetic flux transport over the solar surface; it then reconstructs the TSI from the modelled magnetic features using the SATIRE procedure [23,24]. In both cases, the last datum point (for 2019) shown in figure 14 is the observed value from the PMOD composite and in both cases is consistent with the reconstructions. Because these PMOD observations include the quiet Sun, but the reconstructions do not, we can add our ΔQ values from figure 13 (which are by definition zero for 2019). The resulting reconstructions of the combined variations due to the magnetic features and the quiet Sun, $\text{TSI}_m + \Delta Q$, are shown in figure 14b,c. In both cases, the line uses the median value of ΔQ for each year and the grey area bounds the maximum and the minimum in each year from the ensemble shown in figure 13. Note that the dominant uncertainty in the models, TSI_m, was almost certainly the assumption that the quiet-Sun irradiance was constant ($\Delta Q = 0$) and, on that basis, the uncertainties in ΔQ are valuable estimates of the uncertainties in $\text{TSI}_m + \Delta Q$.

6. Discussion and conclusion

SEA11 [4] and *EEA18* [5] have postulated that changes in the quiet-Sun irradiance Q introduced considerable changes in the TSI. Figure 2 shows that their reconstructions are predicting changes in TSI of ΔQ_{MM} between about 4 and 6 W m^{-2} between 1700 and the present day. The radiative climate forcing associated with this is $\Delta Q_{\text{MM}}(1 - A)/4$ and, using a best estimate of the average
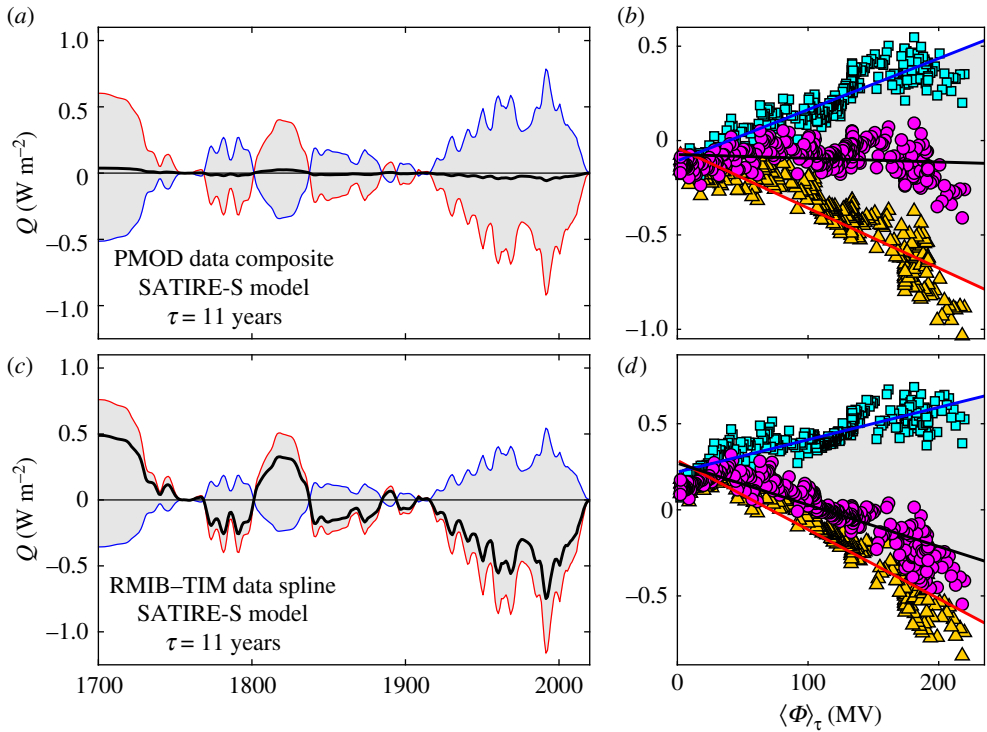
Figure 11. Example of the regression analysis between CR means of the heliospheric modulation potential, averaged over the prior interval of duration $\tau = 11$ years, $\langle \Phi \rangle_\tau$, and the quiet Sun irradiance, Q, derived from the difference between the SATIRE-S model and (a,b) the PMOD data composite and (c,d) the RMIB/TIM data composite. The time series (a,c) are derived from the regression fits given in (b,d). The mauve circles in (b,d) are the data points and are fitted with the linear, ordinary least-squares (OLS) regression line shown in black. The cyan squares are the same data with the addition of a drift factor given by the difference between the blue line in figure 3 and that for the data composite in question (the baseline drift in the ACRIM-3 data), and the blue line is the OLS linear regression fit to these data. For the orange triangles, the added drift is that of the TIM data (w.r.t. the data composite used) and the red line is the OLS regression fit. The black, red and blue lines in (a,c) are the time variations derived from the $\langle \Phi \rangle_\tau$ variation from the three best-fit regression lines shown in (b,d), respectively. (Online version in colour.)

of Earth's planetary albedo from satellite radiation budget experiments of $A = 0.29$ [57], this yields a radiative forcing of between 0.71 and 1.07 W m^{-2} due to such irradiance changes. These estimates are smaller than, but not by a large factor, the best estimated greenhouse gas radiative forcing due to well-mixed carbon dioxide over the same interval of 1.68 ± 0.35 W m^{-2}; by way of context, the total anthropogenic forcing is 2.3 W m^{-2} (with a 5–95% range of 1.1–3.3 W m^{-2}) [58,59]. Other TSI reconstructions based on proxies for solar magnetic structure with no quiet-Sun variation give changes in TSI of between about 0.20 and 0.55 W m^{-2} for the same interval, and these form the basis of the Intergovernmental Panel on Climate Change (IPCC) consensus value. These reconstructions give a solar irradiance radiative forcing $\Delta Q_{MM}(1 - A)/4$ of 0.04–0.10 W m^{-2}. It needs to be stressed at this point that there is overwhelmingly strong evidence from Earth's atmosphere that the larger solar irradiance forcings are unrealistic. The reason is that a TSI increase would heat both the troposphere and the stratosphere whereas data from multiple sources clearly reveal that as the troposphere has warmed the overlying stratosphere has cooled (e.g. [60]), which is a characteristic and unique signature of an enhanced greenhouse effect [61].

The interval of space-based radiometry giving TSI observations is now dominated by the effects of the rapid decline in the long-term variation in solar activity from its peak in 1985 [50] to
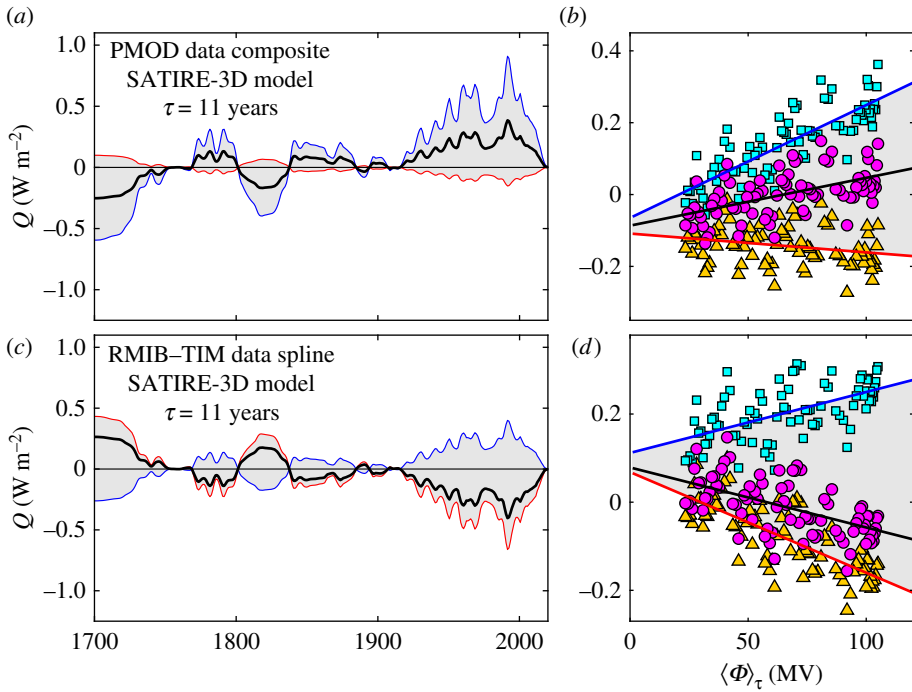
Figure 12. The same as figure 11, but using the SATIRE-3D model. (Online version in colour.)
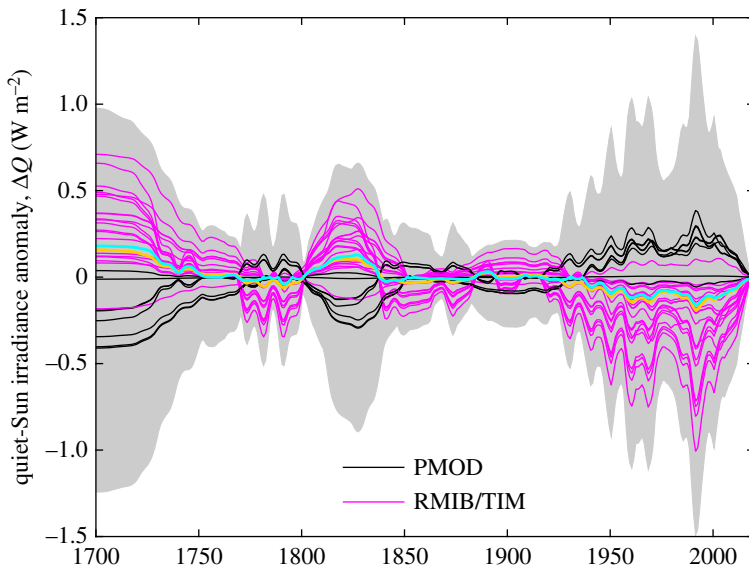

Figure 13. Time variations derived in the way exemplified by figures 11 and 12 for all the model–data combinations listed in table 1. The black lines used the PMOD data composite and the mauve lines the RMIB/TIM data composite (or the TIM or RMIB data individually) and separate lines for $\tau = 11$ years and $\tau = 22$ years. The cyan and orange lines are, respectively, the mean and the median variations for the ensemble of 28 variations. The grey area shows the maximum and minimum values of all the maximum deviations of each ensemble member using the error estimates derived from figure 3 and implemented as shown in figures 1 and 12. (Online version in colour.)
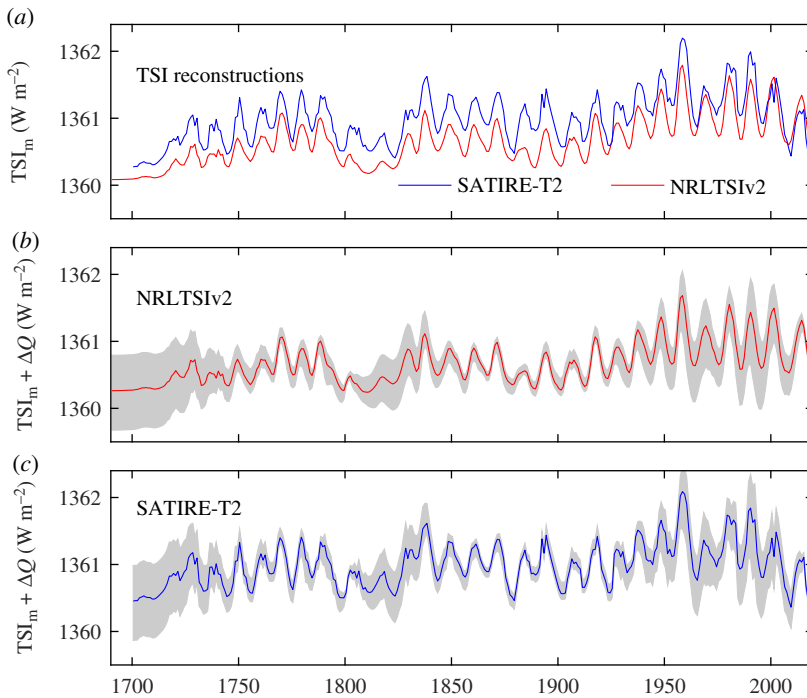
Figure 14. Model reconstructions of TSI since the Maunder minimum. (*a*) Two model reconstructions based on sunspot number, TSI$_m$, the red line giving the NRLTSIv2 reconstruction [56] and the blue line the SATIRE-T2 reconstruction [23,24]. In (*b*) the quiet-Sun irradiance variation $\triangle Q$ shown in figure 13 is added to the NRLTSIv2 reconstruction, and in (*c*) it is added to the SATIRE-T2 reconstruction. In each case, the line is the median value for each year and the grey area is bounded by the maximum and minimum of the set of $\triangle Q$ variations shown in figure 13. The data in the plot are available in the electronic supplementary material. (Online version in colour.)

the present day. We have here restricted our attention to 1995 and after because there is a much greater degree of agreement between the different instruments and data composites—and, during this time, solar activity has shown a steady decline in that both the maxima and the minima of cycles in solar activity indices have declined. In particular, the post-1995 interval avoids the major source of past debates, which has been the difference between ACRIM and PMOD TSI composites caused by the treatment of calibration drift in the data from the Nimbus HF instrument during the short gap (1989–1992) between the self-calibrating ACRIM I and ACRIM II instruments [13,29].

The behaviour of inferred quiet-Sun irradiance variation, Q, depends critically on the data used and not, in general, on the model used. It is interesting to note that the results for the empirical models are generally very similar to those obtained using SATIRE-3D and SATIRE-S for the same observation data series, indicating that overfitting has not been a major problem with the empirical fits and that the quiet-Sun variation has not been falsely attributed to a different factor to any great extent. Hence, the major uncertainty remains the stability of the instruments.

Two contrary behaviours are found and both are entirely feasible. Most of the reconstructions using PMOD data result in a maximum in Q during the MGSM and minima in Q during both the Dalton and Maunder minima. In polarity (but not in magnitude as discussed below), this is consistent with the *SEA11* [4] and *EEA18* [5] postulated variations of Q. For this to be the case, the regions on the solar surface causing quiet-Sun fluctuations in irradiance would have to extend outside the regions where active regions appear, to the extent that the appearance of active regions does not reduce the enhancement of the quiet-Sun emission.

On the other hand, all bar one of the reconstructions using TIM or RMIB data (or a composite of the two) result in a minimum in Q during the MGSM and maxima in Q during the Dalton and Maunder minima. This is inconsistent with the polarity of the effect in the *SEA11* [4] and *EEA18* [5] postulate. This 'opposite-polarity effect' (giving enhanced Q during the Maunder and Dalton minima) could be explained if the postulated residual weak magnetic patches causing the variation in Q during the activity minima were the same regions that at high solar activity became active regions, such that when active regions re-appear they replace significant fractions of the areas giving raised Q, causing Q to fall as solar activity increases. Alternative explanations would be that the solar radius increases during low-activity intervals or the limb darkening is reduced. There is a growing consensus on the observational drift of the instruments, revealed in figure 3. This tends to support higher stability for the RMIB and TIM data, as opposed to that for PMOD, and hence we infer that the opposite-polarity effect probably applies. Note that a symptom of the fundamental difference in the general behaviour for the PMOD data and the TIM and/or RMIB data can be identified in figure 1*d*: for the PMOD data, the TSI during the solar minimum at the end of solar cycle 24 (around 2019) is lower than that for the solar minimum between cycles 23 and 24 (around 2008/2009), whereas for the TIM data the converse is true.

The second point to note concerns the magnitudes of the effects that we derive. The values of $\Delta Q_{MM} = Q_{2019} - Q_{MM}$ derived by *SEA11* [4] and *EEA18* [5] were about $6\,\mathrm{W\,m}^{-2}$ and about $4\,\mathrm{W\,m}^{-2}$, respectively. We here find much smaller values. The mean and median of the ensemble of 28 reconstructions we derive are near $-0.2\,\mathrm{W\,m}^{-2}$. The range covered by the 28-member ensemble of best-fit regressions is between -0.7 and $0.4\,\mathrm{W\,m}^{-2}$ and the full uncertainty range, allowing for the estimated range of instrumental drifts, is between -0.95 and $1.25\,\mathrm{W\,m}^{-2}$. *EEA18* do make it clear that their result depends critically on the scaling factor between the quiet-Sun irradiance and the smoothed prior value of the heliospheric modulation parameter. Using a range of data and models, we find that *EEA18* overestimate that sensitivity factor by a factor of about 5 and we find that it is likely even to have the opposite polarity to that found by *EEA18*. *EEA18* note that differences used to scale their variation is lost in the noise of the TSI observations and, given that we find that even the polarity of the drift depends on which data are used, we agree. But *EEA18* do not point out the implications of fitting when noise levels are so high for the validity of their reconstruction: we here find that the long-term change in Q that they derive is considerably outside a realistic uncertainty band.

The SATIRE-3D modelling is of great significance. This is the first TSI model to be fully independent of the observed variation (only the zero-level offset is adjusted to match the observations). This modelling is only available for a short interval, but the variation it generates is extremely close to the TIM observations. It is also the first attempt at such TSI modelling and so improvements are likely in the future; however, we find it strongly supports the TIM data and hence the variations in Q that are opposite in sense to those invoked by *SEA11* [4] and *EEA18* [5]. We also note that there is a growing consensus around the TIM data in terms of agreement with other instruments. This leads to the conclusions that the decline in the ACRIM-III TSI observations is an instrumental effect and not a real phenomenon and the same is probably true of the lesser decline in values of the PMOD composite.

In summary, our analysis does not replicate the extremely large changes (ΔQ_{MM} of $4–6\,\mathrm{W\,m}^{-2}$) in the quiet-Sun contribution to TSI postulated by Shapiro *et al.* [4] and Egorova *et al.* [5]. These values yield a radiative climate forcing since 1700 of $\Delta Q_{MM}(1-A)/4$ of between 0.71 and $1.07\,\mathrm{W\,m}^{-2}$. From figure 13, the maximum uncertainties in ΔQ_{MM} give values of 1.25 and $-1.0\,\mathrm{W\,m}^{-2}$, which yield climate radiative forcings since 1700 of 0.22 and $-0.18\,\mathrm{W\,m}^{-2}$. The ensemble of 28 reconstructions presented here gives a range in ΔQ_{MM} between 0.40 and $-0.75\,\mathrm{W\,m}^{-2}$, which yields a range of climate radiative forcings since 1700 of between 0.07 and $-0.13\,\mathrm{W\,m}^{-2}$. Reconstructions that add our estimates of the quiet-Sun variation to models of the TSI variation due to sunspots and faculae (figure 14) are available in the electronic supplementary material.

are available from https://www.ncei.noaa.gov/thredds/catalog/cdr-total-solar-irradiance/daily/catalog.html. The annual NRLTSIv2 model reconstruction is available from https://www.ncei.noaa.gov/thredds/catalog/cdr-total-solar-irradiance/yearly/catalog.html. The SORCE/TIM observations are available from http://lasp.colorado.edu/home/sorce/data/. The ACRIM3 data (version May 2011) are available from http://www.acrim.com/RESULTS/data/acrim3/acrim3_sdc_ts_1104.rtf. The PMOD data composite is available from ftp://ftp.pmodwrc.ch/pub/data/irradiance/composite/DataPlots/composite_42_65_1709.dat. The RMIB data composite (version 20161010) is available from ftp://gerb.oma.be/steven/RMIB_TSI_composite/RMIB_TSI_composite_latest.txt. The Community Composite (v. 01) is available from https://spot.colorado.edu/~koppg/TSI/Thierry_TSI_composite.txt. The TCTE data are available from http://lasp.colorado.edu/lisird/data/tcte_tsi_24hr/. The TSIS data are available from http://lasp.colorado.edu/lisird/data/tsis_ssi_24hr/. The SOVAP data are available from https://www.researchgate.net/profile/Mustapha_Meftah/publication/308676535_SOVAP_PICARD_Composite_V1/data/57ea9c2f08ae5d93a481536e/SOVAP-PICARD-Composite-V1.txt. Monthly means of heliospheric modulation potential Φ are given for 1951–2016 in table 2 of Usoskin et al. [46]. These have been extended to 2019 using data from neutron monitors obtained from http://www01.nmdb.eu/nest/. Annual means of reconstructed cosmic ray counts for 1611–2008 based on Usoskin et al. [44] are available from http://www1.ncdc.noaa.gov/pub/data/paleo/climate_forcing/solar_variability/usoskin-cosmic-ray.txt.

References

1. Gray LJ et al. 2010 Solar influences on climate. Rev. Geophys. **48**, RG4001. (doi:10.1029/2009RG000282)
2. Solanki SK, Krivova NA, Haigh JD. 2013 Solar irradiance variability and climate. Annu. Rev. Astron. Astrophys. **51**, 311–351. (doi:10.1146/annurev-astro-082812-141007)
3. Owens MJ, Lockwood M, Hawkins E, Usoskin IG, Jones GS, Barnard LA, Schurer A, Fasullo J. 2017 The Maunder minimum and the Little Ice Age: an update from recent reconstructions and climate simulations. J. Space Weather Space Clim. **7**, A33. (doi:10.1051/swsc/2017034)
4. Shapiro AI, Schmutz W, Rozanov E, Schoell M, Haberreiter M, Shapiro AV, Nyeki S. 2011 A new approach to the long-term reconstruction of the solar irradiance leads to large historical solar forcing. Astron. Astrophys. **529**, 1–8. (doi:10.1051/0004-6361/201016173)
5. Egorova T, Schmutz W, Rozanov E, Shapiro AI, Usoskin I, Beer J, Tagirov RV, Peter T. 2018 Revised historical solar irradiance forcing. Astron. Astrophys. **615**, 1–10. (doi:10.1051/0004-6361/201731199)
6. Hickey JR, Alton BM, Kyle HL, Hoyt D. 1988 Total solar irradiance measurements by ERB/Nimbus-7. A review of nine years. Space Sci. Rev. **48**, 321–334. (doi:10.1007/BF00226011)
7. Kyle HL, Hoyt DV, Hickey JR, Maschhoff RH, Vallette BJ. 1993 Nimbus-7 Earth radiation budget calibration history. Part 1: The solar channels. NASA Report NASA-RP-1316, REPT-93B00110, NAS 1.61:1316. See http://hdl.handle.net/2060/19940009490
8. Fröhlich C, Lean J. 1998 The Sun's total irradiance: cycles and trends in the past two decades and associated climate change uncertainties. Geophys. Res. Lett. **25**, 4377–4380. (doi:10.1029/1998gl900157)
9. Ball WT, Schmutz W, Fehlmann A, Finsterle W, Walter B. 2016 Assessing the beginning to end-of-mission sensitivity change of the PREcision MOnitor Sensor total solar irradiance radiometer (PREMOS/PICARD). J. Space Weather Space Clim. **6**, A32. (doi:10.1051/swsc/2016026)
10. Fröhlich C. 2007 Solar irradiance variability since 1978. Space Sci. Rev. **125**, 53–65. (doi:10.1007/s11214-006-9046-5)
11. Mekaoui S, Dewitte S. 2008 Total solar irradiance measurement and modelling during cycle 23. Solar Phys. **247**, 203–216. (doi:10.1007/s11207-007-9070-y)

12. Willson RC. 2014 ACRIM3 and the total solar irradiance databases. *Astrophys. Space Sci.* **352**, 341–352. (doi:10.1007/s10509-014-1961-4)

13. Lockwood M, Frölich C. 2008 Recent oppositely directed trends in solar climate forcings and the global mean surface air temperature. II. Different reconstructions of the total solar irradiance variation and dependence on response time scale. *Proc. R. Soc. A* **464**, 1367–1385. (doi:10.1098/rspa.2007.0347)

14. Dudok de Wit TD, Kopp G, Fröhlich C, Scholl M. 2017 Methodology to create a new total solar irradiance record: making a composite out of multiple data records. *Geophys. Res. Lett.* **44**, 1196–1203. (doi:10.1002/2016gl071866)

15. Yeo KL, Krivova NA, Solanki SK, Glassmeier KH. 2014 Reconstruction of total and spectral solar irradiance from 1974 to 2013 based on KPVT, SoHO/MDI, and SDO/HMI observations. *Astron. Astrophys.* **570**, 1–18. (doi:10.1051/0004-6361/201423628)

16. Kopp G, Lawrence G, Rottman G. 2005 The total irradiance monitor (TIM): science results. *Solar Phys.* **230**, 129–139. (doi:10.1007/s11207-005-7433-9)

17. Meftah M, Chevalier A, Conscience C, Nevens S. 2016 Total solar irradiance as measured by the SOVAP radiometer onboard PICARD. *J. Space Weather Space Clim.* **6**, 1–8. (doi:10.1051/swsc/2016027)

18. Krivova NA, Vieira LEA, Solanki SK. 2010 Reconstruction of solar spectral irradiance since the Maunder minimum. *J. Geophys. Res.* **115**, A12112. (doi:10.1029/2010JA015431)

19. Yeo KL, Krivova NA, Solanki SK. 2014 Solar cycle variation in solar irradiance. *Space Sci. Rev.* **186**, 137–167. (doi:10.1007/s11214-014-0061-7)

20. Coddington O *et al.* 2019 Solar irradiance variability: comparisons of models and measurements. *Earth Space Sci.* **6**, 2525–2555. (doi:10.1029/2019EA000693)

21. Krivova NA, Solanki SK, Fligge M, Unruh YC. 2003 Reconstruction of solar irradiance variations in cycle 23: is solar surface magnetism the cause? *Astron. Astrophys.* **399**, L1–L4. (doi:10.1051/0004-6361:20030029)

22. Yeo KL, Solanki SK, Norris CM, Beeck B, Unruh YC, Krivova NA. 2017 Solar irradiance variability is caused by the magnetic activity on the solar surface. *Phys. Rev. Lett.* **19**, 091102. (doi:10.1103/PhysRevLett.119.091102)

23. Dasi-Espuig M, Jiang J, Krivova NA, Solanki SK. 2014 Modelling total solar irradiance since 1878 from simulated magnetograms. *Astron. Astrophys.* **570**, A23. (doi:10.1051/0004-6361/201424290)

24. Dasi-Espuig M, Jiang J, Krivova NA, Solanki SK, Unruh Y, Yeo KL. 2016 Reconstruction of spectral solar irradiance since 1700 from simulated magnetograms. *Astron. Astrophys.* **590**, A63. (doi:10.1051/0004-6361/201527993)

25. Wu C-J, Krivova NA, Solanki SK, Usoskin IG. 2018 Solar total and spectral irradiance reconstruction over the last 9000 years. *Astron. Astrophys.* **620**, A120. (doi:10.1051/0004-6361/201832956)

26. Eddy JA. 1976 The Maunder minimum. *Science* **192**, 1189–1202. (doi:10.1126/science.192.4245.1189)

27. Usoskin IG *et al.* 2015 The Maunder minimum (1645–1715) was indeed a Grand minimum: a reassessment of multiple datasets. *Astron. Astrophys.* **581**, A95. (doi:10.1051/0004-6361/201526652)

28. Lockwood M, Owens MJ, Hawkins E, Jones GS, Usoskin IG. 2017 Frost fairs, sunspots and the Little Ice Age. *Astron. Geophys.* **58**, 2.17–2.23. (doi:10.1093/astrogeo/atx057)

29. Scafetta N, Willson RC, Lee JN, Wu DL. 2019 Modeling quiet solar luminosity variability from TSI satellite measurements and proxy models during 1980–2018. *Remote Sens.* **11**, 2569. (doi:10.3390/rs11212569.)

30. McCracken KG, McDonald FB, Beer J, Raisbeck G, Yiou F. 2004 A phenomenological study of the long-term cosmic ray modulation, 850–1958 AD. *J. Geophys. Res.* **109**, A12103. (doi:10.1029/2004JA010685)

31. Usoskin IG, Gallet Y, Lopes F, Kovaltsov GA, Hulot G. 2016 Solar activity during the Holocene: the Hallstatt cycle and its consequence for grand minima and maxima. *Astron. Astrophys.* **587**, 1–10. (doi:10.1051/0004-6361/201527295)

32. Judge PG, Lockwood GW, Radick RR, Henry GW, Shapiro AI, Schmutz W, Lindsey C. 2012 Confronting a solar irradiance reconstruction with solar and stellar data. *Astron. Astrophys.* **544**, 1–6. (doi:10.1051/0004-6361/201218903)

33. Lockwood M. 2006 What do cosmogenic isotopes tell us about past solar forcing of climate? *Space Sci. Rev.* **125**, 95–109. (doi:10.1007/s11214-006-9049-2)

34. Lockwood M. 2004 Solar outputs, their variations and their effects of Earth. In *The sun, solar analogs and the climate. Proceedings of Saas-Fee advanced course* (eds I Rüedi, M Güdel, W Schmutz), pp. 107–304. Berlin, Germany: Springer.

35. Lockwood M, Stamper R, Wild MN. 1999 A doubling of the sun's coronal magnetic field during the last 100 years. *Nature* **399**, 437–439. (doi:10.1038/20867, 1999)

36. Solanki SK, Schüssler M, Fligge M. 2000 Evolution of the Sun's large-scale magnetic field since the Maunder minimum. *Nature* **408**, 445–447. (doi:10.1038/35044027)

37. Lockwood M. 2003 Twenty-three cycles of changing open solar flux. *J. Geophys. Res.* **108**, 1128. (doi:10.1029/2002JA009431)

38. Lockwood M. 2013 Reconstruction and prediction of variations in the open solar magnetic flux and interplanetary conditions. *Living Rev. Sol. Phys.* **10**, 4. (doi:10.12942/lrsp-2013-4)

39. Owens MJ *et al.* 2016 Near-Earth heliospheric magnetic field intensity since 1800. Part 2: cosmogenic radionuclide reconstructions. *J. Geophys. Res.* **121**, 6064–6074. (doi:10.1002/2016JA022550)

40. Steinhilber F, Beer J, Fröhlich C. 2009 Total solar irradiance during the Holocene. *Geophys. Res. Lett.* **36**, L19704. (doi:10.1029/2009GL040142)

41. Ball WT, Unruh YC, Krivova NA, Solanki S, Wenzler T, Mortlock DJ, Jaffe AH. 2012 Reconstruction of total solar irradiance 1974–2009. *Astron. Astrophys.* **541**, A27. (doi:10.1051/0004-6361/201118702)

42. Kopp G. 2014 An assessment of the solar irradiance record for climate studies. *J. Space Weather Space Climate* **4**, A14. (doi:10.1051/swsc/2014012)

43. Kopp G. 2016 Magnitudes and timescales of total solar irradiance variability. *J. Space Weather Space Clim.* **6**, 1–11. (doi:10.1051/swsc/2016025)

44. Usoskin IG, Mursula K, Solanki SK, Schussler M, Kovaltsov GA. 2002 A physical reconstruction of cosmic ray intensity since 1610. *J. Geophys. Res.* **107**, 1374. (doi:10.1029/2002JA009343).

45. Lockwood M, Nevanlinna H, Barnard L, Owens MJ, Harrison RG, Rouillard AP, Scott CJ. 2014 Reconstruction of geomagnetic activity and near-Earth interplanetary conditions over the past 167 years: 4. Near-Earth solar wind speed, IMF, and open solar flux. *Ann. Geophys.* **32**, 383–399. (doi:10.5194/angeo-32-383-2014)

46. Usoskin IG, Gil A, Kovaltsov GA, Mishev AL, Mikhailov VV. 2017 Heliospheric modulation of cosmic rays during the neutron monitor era: calibration using PAMELA data for 2006–2010. *J. Geophys. Res. Space Physics* **122**, 3875–3887. (doi:10.1002/2016JA023819)

47. Usoskin IG. 2017 A history of solar activity over millennia. *Living Rev. Sol. Phys.* **14**, 3. (doi:10.1007/s41116-017-0006-9)

48. Owens MJ *et al.* 2016 Near-Earth heliospheric magnetic field intensity since 1800. Part 1: sunspot and geomagnetic reconstructions. *J. Geophys. Res.* **121**, 6048–6063. (doi:10.1002/2016JA022529)

49. Lockwood M, Owens MJ. 2014 Centennial variations in sunspot number, open solar flux and streamer belt width: 3. Modelling. *J. Geophys. Res. Space Physics* **119**, 5193–5209. (doi:10.1002/2014JA019973)

50. Lockwood M, Frölich C. 2007 Recent oppositely directed trends in solar climate forcings and the global mean surface air temperature. *Proc. R. Soc. A* **463**, 2447–2460. (doi:10.1098/rspa.2007.1880)

51. Lockwood M, Rouillard AP, Finch ID. 2009 The rise and fall of open solar flux during the current grand solar maximum. *Astrophys. J.* **700**, 937–944. (doi:10.1088/0004-637X/700/2/937)

52. Usoskin IG, Solanki SK, Schüssler M, Mursula K, Alanko K. 2003 Millennium-scale sunspot number reconstruction: evidence for an unusually active Sun since the 1940s. *Phys. Rev. Lett.* **91**, 211101. (doi:10.1103/PhysRevLett.91.211101)

53. Clette F, Svalgaard L, Vaquero JM, Cliver EW. 2014 Revisiting the sunspot number. *Space Sci. Rev.* **186**, 35–103. (doi:10.1007/s11214-014-0074-2)

54. Meng X-I, Rosenthal R, Rubin DB. 1992 Comparing correlated correlation coefficients. *Psychol. Bull.* **111**, 172–175. (doi:10.1037//0033-2909.111.1.172)

55. Lockwood M, Bentley S, Owens MJ, Barnard LA, Scott CJ, Watt CE, Allanson O. 2018 The development of a space climatology: 1. Solar-wind magnetosphere coupling as a function of timescale and the effect of data gaps. *Space Weather* **17**, 133–156. (doi:10.1029/2018SW001856)

56. Coddington O, Lean JL, Pilewskie P, Snow M, Lindholm D. 2016 A solar irradiance climate data record. *Bull. Am. Meteor. Soc.* **97**, 1265–1282. (doi:10.1175/BAMS-D-14-00265.1)

57. Stephens GL, O'Brien D, Webster PJ, Pilewski P, Kato S, Li J. 2015 The albedo of Earth. *Rev. Geophys.* **53**, 141–163. (doi:10.1002/2014RG000449)
58. Intergovernmental Panel on Climate Change. 2013 Summary for policymakers. In *Climate change 2013: the physical science basis. Contribution of Working Group I to the fifth assessment report of the Intergovernmental Panel on Climate Change* (ed. TF Stocker *et al.*). Cambridge, UK: Cambridge University Press.
59. Myhre G *et al.* 2013 Anthropogenic and natural radiative forcing. In *Climate change 2013: the physical science basis. Contribution of Working Group I to the fifth assessment report of the Intergovernmental Panel on Climate Change* (eds TF Stocker *et al.*), pp. 659–740. Cambridge, UK: Cambridge University Press.
60. Shangguan M, Wuke W, Shuanggen J. 2019 Variability of temperature and ozone in the upper troposphere and lower stratosphere from multi-satellite observations and reanalysis data. *Atmos. Chem. Phys.* **19**, 6659–6679. (doi:10.5194/acp-19-6659-2019)
61. Ramaswamy V, Schwarzkopf MD, Randel WJ, Santer BD, Soden BJ, Stenchikov GL. 2006 Anthropogenic and natural influences in the evolution of lower stratospheric cooling. *Science* **311**, 1138–1141. (doi:10.1126/science.1122587)